Size-controllable Growth of ZnO Nanorod Arrays and Their Surface Modifications

ZnO 納米柱陣列可控生長與表面修飾

JIAO, Yang

A Thesis Submitted in partial Fulfillment
of the Requirements for the Degree of
Doctor of Philosophy
in
Materials Science and Engineering

The Chinese University of Hong Kong

May 2010

Thesis/Assessment Committee

Professor NG, Hang Leung Dickon (Chair)
Professor LI, Quan (Thesis Supervisor)
Professor WANG, Jianfang (Committee Member)

Abstract

One dimensional (1D) ZnO nanostructure becomes a research focus in recent years. On the one hand, ZnO itself possesses structural, electrical and optical properties that make it useful for a diverse range of technological applications. On the other hand, semiconductor nanowire owns many advantages, such as superiority in electron transport and its high surface to volume ratio. Aligned ZnO 1D nanostructures on conducting substrates are of special interests, as they are easy to be integrated into devices, directly working as functional unit.

In this study, a solution chemistry based method to grow aligned ZnO nanorod arrays on Zn foil is developed at first. Effects of various growth parameters, including the temperature, solution composition and the concentration of individual components on the morphology, structural quality, and properties of the ZnO nanorods are studied. The average diameter of the nanorods in the array can be tuned from ~20 nm to ~150 nm by systematically changing the growth conditions. Nanorods with larger diameters are found to be of better structural quality as compared to the smaller diametered ones, as suggested by the cathodoluminescence measurement. Following similar logic, a vapor transport deposition route on controllable fabricating of the ZnO nanorod arrays is investigated. The average diameter of the ZnO nanorods can be tuned from less than 40 nm to larger than submicron, by controlling the fabrication conditions. Larger-diametered nanorods that grow on higher temperature zone are found to possess higher band edge to defect emission ratio.

Green emission is observed from the ZnO nanorods synthesized by both methods, which is commonly attributed to the surface defect emission from the nanostructure. We modify surface of the nanorods with SiO_2 and investigate the

relation between green emission and the surface defect. However, the surface passivation fails to reduce the green emission significantly, suggesting that surface defects of ZnO are not necessarily responsible for the green emission, but the interior structure quality of the ZnO nanorods decides the luminescence behavior.

At last, a thermal evaporation method that modifies the surface of ZnO nanorods and forms core shell structure is developed, which structure constitutes the photoelectrode for solar energy application. Single crystal ZnO nanorods are uniformly covered by wurtzite polycrystalline $Cd_xZn_{1-x}S_ySe_{1-y}$ layer. The band gap of the shell can be systematically tuned from 2.5 to 1.7 eV by varying its composition, as suggested by the optical extinction measured of the samples. The type II band alignment between the ZnO core and the alloy shell enables effective photo-generated charge carrier separation, and the single crystalline ZnO nanorod array provides a direct electrical pathway for the photo-injected electron transport. The nanocable solar cells exhibited short-circuit current ~0.2 mA/cm^2 and open-circuit voltages of 0.45 V when illuminated with 100 mW/cm^2 simulated AM 1.5 spectrum.

摘 要

一維 ZnO 納米結構是近年來的一個研究熱點。一方面由於 ZnO 本身在結構、電學、光學方面的性質使得它適合多種技術應用。另一方面，半導體納米線具有很多優勢，比如有利於電子輸運和高的比表面積。直接生長在導電襯底上的一維 ZnO 納米結構陣列更受青睞，因為它更易於組裝成器件，同時直接作為一個功能單元。

我們首先研究了一種基於溶液化學的在 Zn 片上生長 ZnO 納米柱陣列的方法。研究了各種生長條件包括溫度、溶液配比、溶液各成份的濃度對 ZnO 納米柱的形貌、結構品質及性質的影響。通過系統地調節其生長條件，陣列中納米柱的平均直徑可以從 ~20 nm 調節到~150 nm。陰極螢光譜的測量發現相對於直徑較細的納米柱，直徑較粗的納米柱有更好的結構品質。按照類似的思路，我們還研究了用氣相傳輸沉積的方法控制 ZnO 納米柱陣列的生長。陣列中納米柱的平均直徑從 ~40 nm 到接近 500 nm 可調。直徑較粗的且生長在較高溫區的納米柱顯示出較高的帶邊/缺陷發光比值。

用以上兩種方法製備的 ZnO 納米柱都有綠色螢光。綠色螢光通常被歸結為納米結構的表面缺陷發光。我們用 SiO_2 包覆 ZnO 納米柱的表面，研究綠色螢光與其表面缺陷的關係。然而表面鈍化並沒有使綠色螢光減弱很多，表明綠色螢光並不一定由表面缺陷引起，而 ZnO 納米柱的內在品質才是決定其螢光行為的關鍵。

最後我們研究了一種通過熱蒸發沉積的方式修飾 ZnO 納米柱表面並形成核殼結構的方法。而該結構適合作為太陽能電池的光電極。在這種結構中，單晶 ZnO 納米柱表面均勻地包裹著多晶 $Cd_xZn_{1-x}S_ySe_{1-y}$ 合金層。通過改變合金殼層的成份比，該層的帶寬可以從 2.5eV 調節到 1.7eV。ZnO 內核與合金殼層之間的 II 型接觸有效地促使光生電子空穴對的分離；單晶 ZnO 納米柱則為光生電子提供了直接的輸運通道。用這種核殼結構組裝的太陽能電池在 100mW/cm² AM1.5 光照下產生~0.2mA/cm²的短路電流與 0.45V 開路電壓。

Acknowledgement

I would like to acknowledge my supervisor, Prof. Quan Li, for her patient guidance and helpful suggestions in my study.

Sincere thanks are given to the staff in Central Lab, Mr. Andrew Li and Mr. M. H. Yeung, for their instrumental assistance.

I would like to thank my groupmates, Dr. Wang Juan, Dr. Shi Liang, Mr. Zhu Haojun, Mr. Xu Yeming, Mr. Wang Xiao feng, and Mr. Zhou Min jie, for their sincere help and encouragement.

Table of Contents

List of Figures

List of Tables

Chapter 1 Introduction

ZnO has gained substantial interest in the research community for many decades as a multi-functional semiconductor material [1]. It possesses direct wide band gap (~ 3.37 eV at room temperature), large exciton binding energy (60 meV) and high piezoelectric constant (d_{33}=246), which facilitate the studies to employ it as transparent electrode, light emitting material, especially room temperature UV lasing material, and piezoelectric transducer, etc. [2-5]. Current simple crystal-growth technology for ZnO further results in a potentially lower cost for ZnO-based devices [1]. Moreover, it is environmentally stable as well as biocompatible [6]. Successful fabrication of ZnO nanostructures in recent years [2-5] and its possible development with the continuous advancement of nanotechnology further fuels the research on this material.

Research interest on quasi-one-dimensional (quasi-1D) ZnO nanostructures is promoted by the inspiring idea of building electronic devices at the nanometer scale using the bottom-up approach, as they are expected to serve as both the functional units and the wires that access them. Besides the possibility of exploring quantum effects at the nanoscopic scale, the quasi-1D system could exhibit its superiority to the bulk material even at the mesoscopic scale, where the lateral size falls below the carrier diffusion length. In such case, the unnecessary lateral transport and the

resulting recombination loss are eliminated, which leads to a reduction on the nonradiative recombination and carrier scattering loss. Besides free standing quasi-1D ZnO nanostructures, aligned ZnO 1D nanostructures on conducting substrates are of special interests, as they are easy to be integrated into devices, directly working as functional unit, for instance, nanoelectrode for many optoelectronic applications[7], nanoprobe for gas sensing [8].

In the present study, we focus at technologies on controllable fabricating aligned ZnO nanorod arrays on conductive substrates, as well as surface modification of the nanorod arrays.

Chapter 2 briefly reviews the studies on ZnO 1D nanostructres in recent years, including their synthesis methods, growth mechanisms, properties and applications in devices. Chapter 3 describes the equipment and techniques employed for the 1D ZnO nanostructures growth and characterizations. In Chapter 4, we start with investigations on a simple and low cost solution chemistry approach to grow aligned ZnO nanorod arrays. Effects of various growth parameters on the morphology, structural quality, and properties of the ZnO nanorods are investigated. Chapter 5 follows similar logic as chapter 4 to describe a vapor transport deposition route on controllable fabricating of the ZnO nanorod arrays. Green emission is observed from the ZnO nanorods synthesized by both methods, which is commonly attributed

to the surface defect emission from the nanostructure. In chapter 6, we modify surface of the nanorods with SiO_2 and investigate the relation between green emission and the surface defect. In chapter 7, we develop a simple thermal evaporation method to modify the aligned ZnO nanorod arrays' surface with II-VI semiconductors, thus an aligned core-shell heterojunction semiconductor nanorod arrays configuration is demonstrated. The band gap of the shell material can be systematically tuned by varying its composition. Finally, the nanocable configuration is integrated into a proto type solar cell, demonstrating its possibility in application of solar energy conversion. At last, Chapter 8 summarizes the main results of this study.

Chapter 2 Background of One-dimensional ZnO Nanostructures — growth, properties and devices

2.1 Growth methods and mechanisms

Various methods have been developed for synthesis of ZnO 1D structures (nanowire, nanorod, nanotube, etc.) and/or aligned 1D structures, during the last ten years. These methods can generally be sorted to two categories: one is based on vapor transport deposition, and the other is based on solution chemistry.

2.1.1 Vapor transport deposition

The vapor-liquid-solid (VLS) process

In a typical vapor transport and deposition process, ZnO nanowires can be grown on Au-coated substrates by heating a mixture of ZnO and graphite powder under a constant flow of argon [9]. The whole process is usually carried out in a horizontal tube furnace. The mixture powder are ground and transferred to an alumina boat. The Au coated Si substrates and the alumina boat are placed in a small quartz tube. The substrates are typically placed 0.5-10 cm from the center of the boat. This quartz tube is then placed inside the furnace tube, with the center of the alumina boat positioned at the center of the furnace and the substrates placed downstream of an argon flow. The temperature of the furnace is ramped to 900℃ or 925℃ and typically kept at that temperature for 1-30 min under a constant flow

of argon (20-25 standard cubic cm). After the furnace cools to room temperature, ZnO nanowires can be found on the surface of the substrates.

The ZnO nanowires grow follow a vapor-liquid-solid (VLS) mechanism, which is a well-accepted mechanism of nanowire growth via gas phase reaction. The carbothermal reduction of ZnO powder generates Zn and CO vapor. The Zn vapor is transported to, and reacted with, the Au catalyst on silicon substrates to form alloy droplets with relatively low solidification temperature. After that, the droplet is enriched by the vapor source material until it is saturated and the crystalline ZnO nanowire starts to form and grow outward from it. The ZnO forms possibly by the reaction between Zn and CO at a low temperature. The anisotropic crystal growth is promoted by the presence of liquid alloy-solid interface, since the liquid droplet acts as a preferable site continually absorbing the source material from the vapor phase. (The presence of a small amount of CO is not expected to significantly change the Au-Zn phase diagram, at the same time they act as the oxygen source during the ZnO nanowire growth. [9])

Size control of the nanowire diameters is thus achieved by varying the thickness of the thin film Au catalyst. It is also possible to grow thinner wires by using mono dispersed Au colloids dispersed on substrates as catalysts [9].

The vapor-solid (VS) process

In addition to the VLS process, the ZnO 1D structure can also grow following a vapor-solid (VS) process [10]. The Zn vapor is first generated by evaporation, chemical reduction or gas reaction, and is subsequently transported to the substrate. Soon the Zn vapor is oxidized and condenses on the substrate to form ZnO nuclei. The continually provided source material then assembles on the top of the nuclei and grows in outward. The anisotropic growth of the ZnO crystal, i.e., a faster growth rate in the *c*-axis, results 1D morphology of the final product. This can be explained by the "lowest energy" argument, i.e., the hexagonal (0001) plane of ZnO with wurtzite structure is the closest packed plane in the crystal, and the staking along the [0001] direction (*c*-axis) therefore becomes energetically favorable.

2.1.2 Chemical solution method

Wet-chemistry methods to grow ZnO nanowires are appealing because of the low growth temperatures, low cost equipments and good potential for scale-up [11]. The principle of aqueous solution techniques is based on heterogeneous nucleation and subsequent crystal growth on a specific surface. The heterogeneous nucleation is induced in a supersaturated solution at a relatively low degree of supersaturation. The condition of the aqueous solution can be controlled by adjusting the reactant

concentration, growth temperature, and the pH value. The crystal phase of the deposits was mainly determined by the pH of the aqueous solutions. If the pH is in the range 6 to 9, the $Zn(OH)_2$ is predominantly formed. The wurtzite ZnO crystal is formed at pH 9–13. During the progress of the formation of ZnO, the complex ion $Zn(NH_3)_4^{2+}$ or $Zn(OH)_4^{2-}$ was formed first. With an increase in temperature, these complexes will be dehydrated. The ZnO crystal forms a heterogeneous nucleus at the interface between substrate and solution. After that, the crystals begin to grow into the nanorods or nanowires [12]. Since there is no involvement of catalysts or templates to serve as energetic favorable sites for the absorption reactant molecules or to confine the growth direction of the product, it would be reasonable to attribute the 1D shape to the anisotropic growth nature of ZnO crystal [10]. The hexagonal cross-section of the product also suggests its crystalline [0001] growth direction.

2.2 Aligned growth of ZnO 1D structures

Aligned growth of nanowires is a simple but very efficient self-assembly technique for integrating nanowires into nanodevices [13]. In this section, we briefly introduce the mechanisms and techniques for growth of aligned ZnO 1D structures (nanowires and/or nanorod arrays).

The large-scale perfect vertical alignment of ZnO nanowires was firstly

demonstrated on a-plane ($(11\bar{2}0)$ crystal surface) orientated single-crystal aluminium oxide (sapphire) substrates. The general idea of the technique is based on VLS mechanism and epitaxial growth, i.e., using gold nanoparticle catalyst to initiates and guides the nanowire growth, and the epitaxial relationship between ZnO and Al_2O_3 leads to the alignment. Crystal structure of the substrate is crucial for the orientation of nanowires. The very small lattice mismatches between the sapphire substrate and ZnO leads to a successful alignment of ZnO nanowires on the substrate. Flowing the similar strategy, aligned ZnO nanowires have been successfully grown on GaN, AlGaN and AlN substrates [14].

For a nonepitaxial substrate (such as silicon or glass), a textured ZnO thin film that is deposited on top of the substrate and acts as a homoepitaxy nucleation layer is crucial for the nanowires alignment [15]. The textured ZnO layer can be prepared through gas-phase deposition or thermally decomposing zinc acetate at 200-350 °C, the later is relatively low-cost and versatile.

2.3 Properties of the ZnO 1D structures

2.3.1 Luminescence properties

Luminescence property of the ZnO 1D structures is most commonly studied. As a potential material for photonic applications, it is important to evaluate its optical

property. Besides that, it directly reflects the crystal quality and effectively reveals the presence of defects.

Typical luminescence spectrum of ZnO consists of an ultraviolet excitonic emission peak and visible emission peak(s) due to deep level defects. The reported visible emissions from different ZnO samples include red, orange, yellow, green and blue luminescence [16,17]. Among them, the green emission is most commonly observed, and the origin for such a peak remains as the most controversial [18,19]. Multiple origins of such green luminescence (GL) band have been proposed in ZnO samples prepared by different methods. It has been suggested that the GL band with a characteristic fine structure is most likely related to the copper impurities, whereas the featureless GL band could relate to native point defects such as V_O or V_{Zn} [1]. Bulk single crystals and phosphor powders are more likely to exhibit extrinsic impurity related emission, while nanostructures and thin films to intrinsic defects [1,18,20].

2.3.2 Electrical properties

I-V characteristics of single ZnO nanowire and bent nanowire

In order to apply ZnO nanostructures to various electronic devices, it is important to understand its transport properties. Single ZnO nanowire's I-V

(current-voltage) characteristic and that of a bent ZnO nanowire were measured in a multiprobe nanoelectronics measurement system [21]. Creating Ohmic contact between the ZnO nanowire and the probe is a key step for the measurements. He et al. coated the tungsten nanotip with a Ti/Au (30 nm: 30 nm) film to achieve the Ohmic contact.

Figure 2-1 demonstrates the *I–V* characteristics of a ZnO nanowire at various bending angles. At the first contact of the nanowire with the nanotip (Fig. 2-1a), the nanowire was already bent a little because a pushing force was necessary for good electrical contact. The corresponding linear and symmetric *I–V* characteristic shows that the Ti/Au-to-ZnO is an Ohmic contact. As the bending proceeded (Fig. 2-1c, e, and g), the electric current dropped significantly with negative bias (Fig. 2-1d, f, and h, respectively), exhibiting asymmetric *I–V* behaviors with the increased strain. It can be seen clearly that the nanotips were firmly attached to the nanowire without sliding, indicating that the contacts were well retained during the bending process and should not cause any change in contact resistance or contact area under bending. The reverse current dropped severely at reverse bias voltage when the nanowire was bent further. In addition, due to the large elasticity of the nanowire, the measurements were reversible.

The ZnO nanowire under bending shows certain rectifying *I–V* characteristics,

similar to the result for a *p–n* junction. The substantial bending of the nanowire and the absence of a symmetric *I–V* characteristic suggest that electrical transport in the nanowire may be governed by an internal field created by bending.

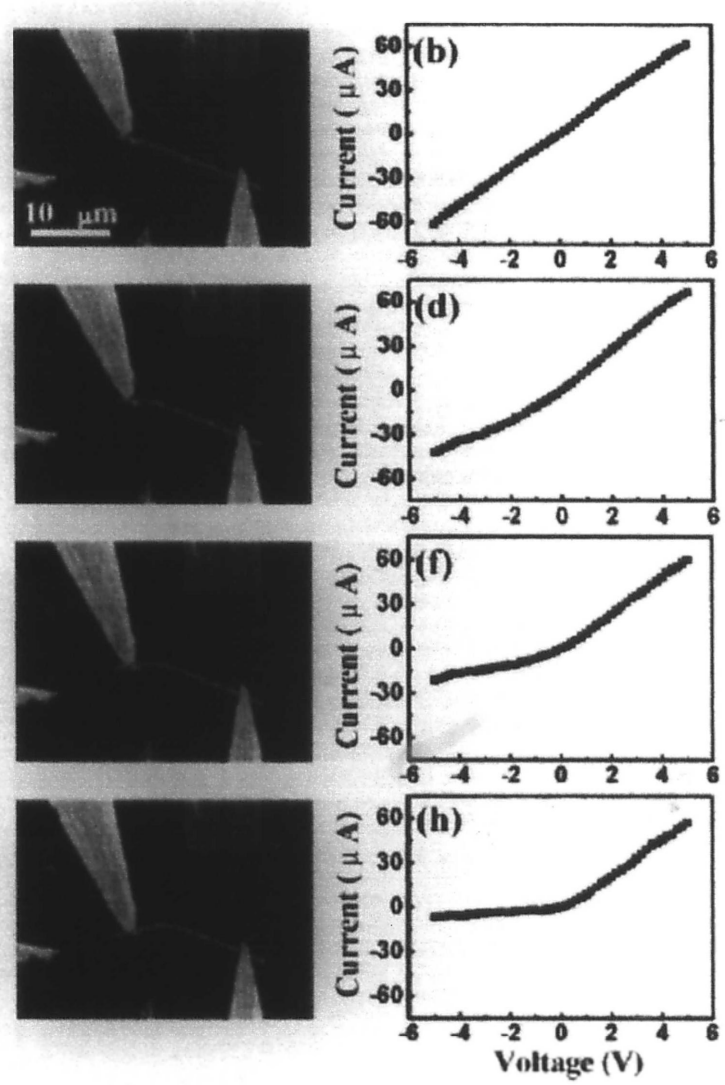

Figure 2- 1 SEM images of one ZnO nanowire at various bending angles (a, c, e, g), and its corresponding *I–V* characteristics (b, d, f, h) [21]

Previous study has shown that a bent ZnO nanowire can produce a piezoelectric field (E_{PZ}) along and across the nanowire due to the strain-induced piezoelectric

effect [22]. Under the displacement of an external force F from the nanotip applied at the surface of the nanowire, the deflection of the ZnO NW creates a strain field. The outer surface is stretched (positive strain e) and the inner surface is compressed (negative e) in the area in contact with the nanotip, as shown in Figure 2-2a.

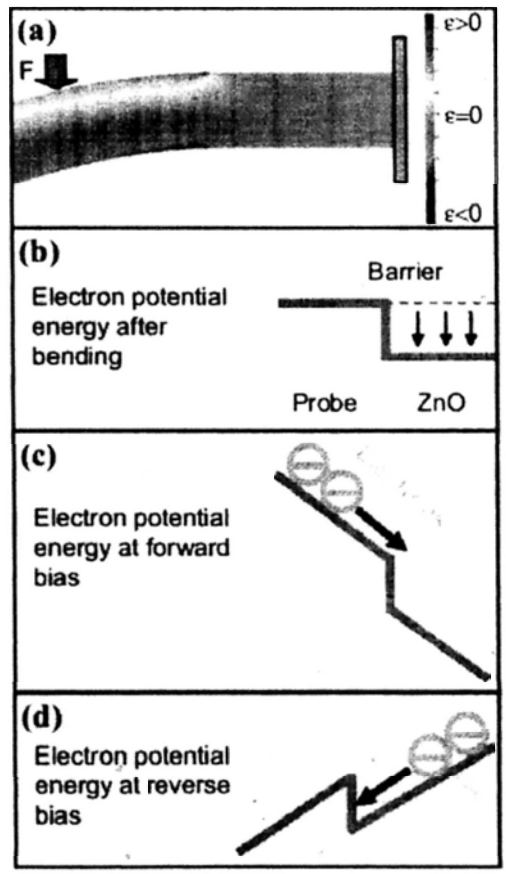

Figure 2- 2 a) Longitudinal strain (e) distribution along a ZnO nanowire as a result of the piezoelectric effect when bent by a nanotip, with the stretched and compressed side surfaces being under positive and negative strain, respectively. Schematic energy diagram of ZnO nanowire accounting for the applied bias and the piezoelectric field. b) Energy barrier built at the nanotip/nanowire interface due to the piezoelectric potential (V^+) at the stretched side. c) Current flow under forward bias. d) Current flow under reverse bias. [21]

The magnitude of the deflection increases with the degree of bending, resulting in an increase in strain field. An electric field E_{PZ} along the nanowire is then created inside the nanowire through the piezoelectric effect, $E_{PZ} = e/d$, where d is the piezoelectric coefficient. The piezoelectric field direction is closely parallel to the nanowire direction (z-axis) at the outer surface and antiparallel to the z-axis at the inner surface. With the increase in bending of the nanowire, the density of the piezoelectric charges on the surface also increases. The potential is created by the relative displacement of the Zn^{2+} cations with respect to the O^{2-} anions, a result of the piezoelectric effect in the wurtzite crystal structure; thus, these ionic charges cannot freely move and cannot recombine without releasing the strain. The potential difference is maintained as long as the deformation is in place. [21]

It is assumed that [21], before bending, there is no energy barrier except for the contact resistance between Ti and ZnO. When the nanotip pushes a nanowire and bends it, a positive potential is produced at the stretched side of the nanowire due to the piezoelectric effect. As a result, an energy barrier is produced at the interface between the tip and the nanowire, with the nanowire being at the higher potential, as illustrated in Figure 2-2b. Note that the actual potential distribution is not fixed due to the nonuniform distribution of strain. However, for ease of comprehension, the potential distribution is simplified here. The schematic diagrams depicting the

principle of operation are shown in Figure 2-2c and d. For the bent ZnO nanowire under forward bias, the electrons have not been blocked by this energy barrier. On the other hand, under reverse bias, electrons need to overcome the energy barrier resulting from the piezoelectric electric field. This energy diagram corresponds well to the result of electric transport measurements on bent ZnO. Such an energy barrier effectively serves as a *p–n* junction barrier at the interface, resisting the current flow from the tip to the nanowire but allowing current to flow from the nanowire to the tip. The magnitude of the barrier increases with the increase in the degree of bending, resulting in a drastic increase of rectifying effect due to the piezoelectric potential energy barrier.

Schottky contact between ZnO nanobelt and Au electrode

Figuring out the interaction between ZnO nanostructures and metal contacts is also a vital issue for applying the nanostructures to various electronic devices. By aligning single ZnO nanobelts/nanowires across paired Au electrodes using dielectrophoresis, rectifying diodes of single nanobelt/nanowire-based devices were fabricated to reveal their electronic properties. [14]

Figure 2-3 shows the *I-V* characteristics of such a device reported by Wang et al. Data correspond to different measurements of the same device at different time

intervals after the device was made. The last measurement was performed 7 days after the device was exposed to air. It is consistent with the data obtained 2 h after the sample was made, showing that the rectifying behavior of the nanodevices is very stable. The temperature dependence of the diode was also measured (Fig. 2-3b). The current under the forward bias decreased with decreasing temperature. The resistivity of the nanobelt increases by a factor of 2 when the temperature decreased from 215 to 104 K, showing a typical semiconductor characteristic.

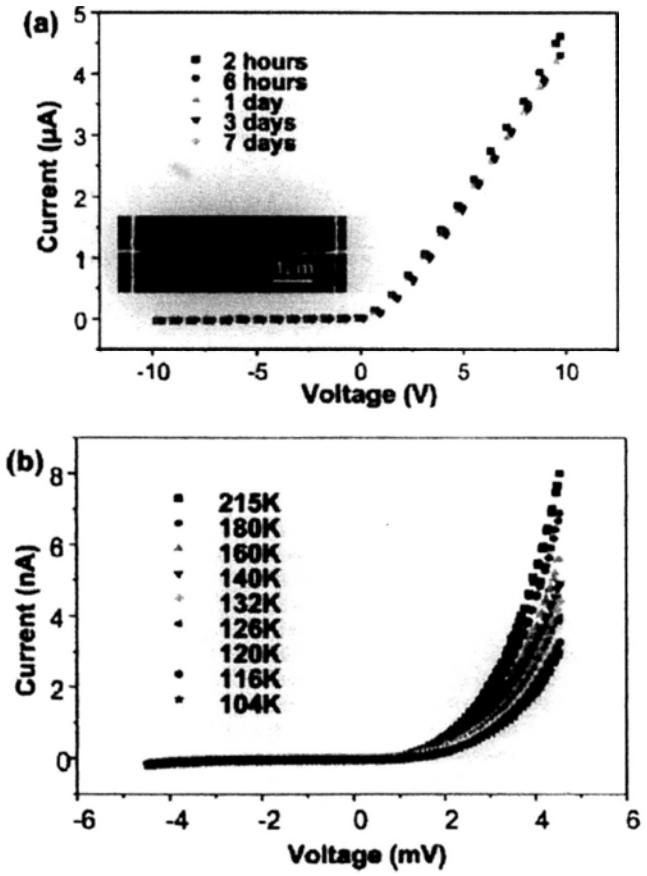

Figure 2- 3 (a) Rectifying IV characteristics of a single ZnO nanobelt lying on Au electrodes at different times after the fabrication, showing the stability of the device. Inset is the SEM image of the ZnO nanobelt device. (b) IV characteristics of the Schottky diode at different temperatures showing the semiconducting behavior. [14]

The diode effect could be a result of the asymmetric contacts between the ZnO nanobelts and the Au electrodes. The ZnO–Au contact is usually a Schottky contact, so there should be no rectifying behavior if the contacts are symmetrical. However, in the dielectrophoresis deposition process, the contacts of the nanobelt's two ends were made one after another onto the corresponding electrodes. It is suspected that the first touched side may have had a firm contact with the electrode and formed a better contact with lower barrier height; whereas the other end that contacted later had a higher barrier, possibly leading to the formation of the Schottky diode for the devices.

Photoconductivity

ZnO nanowire has also exhibited some superb photoconductive properties. Four-terminal measurements of individual ZnO nanowires indicate that they are highly insulating in the dark with a resistivity above 3.5 MΩcm. When the nanowires are exposed to ultraviolet (UV)-light with wavelengths below 380 nm, the nanowire resistivity decreases by typically 4 to 6 orders of magnitude. [23]

Figure 2-4 is reported I-V curves measured on a 60 nm ZnO nanowire in the dark and upon UV-light exposure. A larger photoresponse was detected at higher bias. The I-V curve for the UV-exposed nanowire exhibits nonlinear behavior.

The same nonlinear I-V has been observed for both the wire-on-electrode and electrode-on-wire configurations. The four-terminal and two-terminal measurements show essentially identical resistivity values, which suggests that the Au/ZnO contacts may not contribute to the I-V nonlinearity. The exact reason for this nonlinearity remains unknown at this stage.

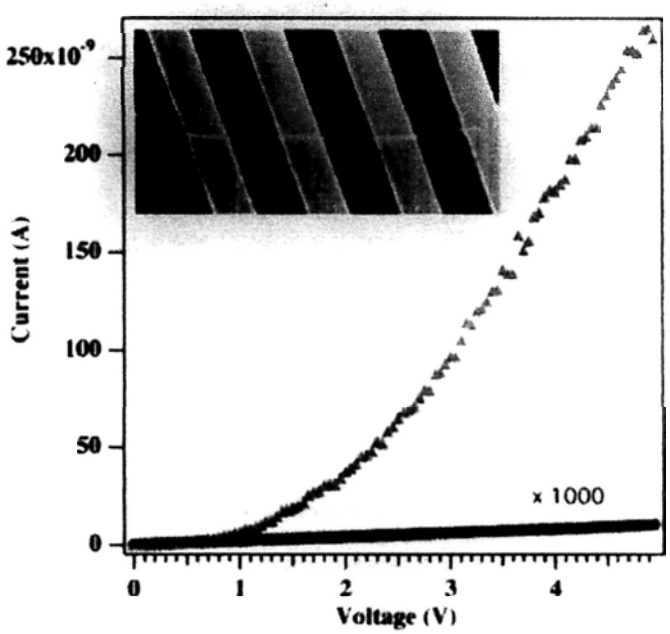

Figure 2- 4 *I-V* curves show dark current (●) and photocurrent (▲) of a single ZnO nanowire under 365 nm, 0.3 $mWcm^{-2}$ UV-light illumination. The inset reveals an FE-SEM image of a 60 nm ZnO nanowire bridging four Au electrodes. The four-terminal I-V measurement is carried out using a Keithley source-measure unit at room temperature. [23]

The nanowire shows high sensitive photoresponse. The photoresponse (I_{pc}) can be expressed by a simple power law

$$I_{pc} \propto P^{0.8} \qquad (2\text{-}1),$$

where P is the power of illumination. The non-unity exponent is a result of the

complex process of electron-hole generation, trapping, and recombination within the semiconductor. Depending on the power of illumination, the resistivity can be reversibly changed by 4 to 6 orders of magnitude without damaging the nanowires.

In addition to the high sensitivity, the nanowire photoconductors also exhibit excellent wavelength selectivity. Green light does not induce a photoresponse, while exposure to less intense UV-light increases the conductivity by 4 orders of magnitude. Measurements of the spectral response show that the ZnO nanowires have a response cut-off wavelength of ~370 nm, which is expected from the wide bandgap (3.37 eV) of ZnO.

It is known that oxygen chemisorption plays a central role in regulating the photosensitivity of bulk or thin film ZnO, where a UV-sensitivity of similar magnitude has been observed. In the dark, oxygen molecules adsorb on the nanowire surface as negatively charged ions by capturing free electrons from the n-type ZnO, thereby creating a depletion layer with low conductivity near the nanowire surface:

$$O_2(g) + e^- \rightarrow O_2^-(ad) \qquad (2\text{-}2)$$

Upon exposure to UV-light, photo-generated holes migrate to the surface and discharge the adsorbed oxygen ions through surface electron-hole recombination:

$$h^+ + O_2^-(ad) \rightarrow O_2(g) \qquad (2\text{-}3)$$

At the same time, the photo-generated electrons significantly increase the conductivity of the nanowire.

2.4 ZnO nanodevices

Zinc oxide possesses structural, electrical and optical properties that make it useful for a diverse range of technological applications [24,25]. The success in preparing many different nanoscale ZnO forms again allows various novel devices to be constructed or proposed. In this section, we briefly introduce several such devices, including their principles, structures, and the superiorities of employing ZnO 1D structures as functional units.

2.4.1 Field effect transistor

The principle of this device is that controlling the gate voltage would control the current flowing from the source to the drain. Field effect transistors were fabricated by depositing dispersed ZnO nanobelts on predefined gold electrode arrays on SiO_2/Si substrate. The SiO_2 gate dielectric thickness was 120 nm and the back gate electrode was fabricated by evaporation of gold on the Si(p+) side of the substrate. By forming metal electrode/nanostructure electrical contacts and capacitively coupling the nanostructure to a nearby gate electrode, a field effect transistor is produced. A typical ZnO field effect transistor showed a gate threshold voltage of

−15 V, a switching ratio of nearly 100 and a peak conductivity of 1.25×10^{-3} (Ω^{-1} cm^{-1}). A completely analogous behavior has been observed in the case of carbon nanotubes deposited on top of Au electrodes or covered by Ti electrodes. Using nanobelt to fabricate field effect transistor allows the exploration of new aspects of the physical and chemical properties of the nanostructures. [26]

2.4.2 Nanocantilevers

The cantilever based scanning probe microscopy (SPM) technique is one of the most powerful approaches in imaging, manipulating and measuring nanoscale properties and phenomena. The most conventional cantilever used for SPM is based on silicon, Si_3N_4 or SiC, which is fabricated by an e-beam or optical lithography technique and has, typically, dimensions of thickness ~100 nm, width ~5 μm and length ~50 μm. Semiconducting 1D nanostructures are ideal candidates for cantilever applications. Structurally they are defect free single crystals, providing excellent mechanical properties. Secondly, their reduced dimensions offer a significant increase in cantilever sensitivity. [26]

Lee *et al.* have proposed the use of well-aligned single-crystalline nanowires for use as sharp atomic force microscopy (AFM) tips. They predict that ZnO nanowires are structurally compatible with AFM cantilevers under typical operating

conditions, and are promising candidates for high-aspect-ratio probes for AFM. Huang *et al.* have characterized the mechanical resonances of a single nanowire using an alternating electric field. They have monitored the flexural mode of the nanowire *in situ* in a transmission electron microscope (TEM). With an elastic bending modulus of ~58 GPa and a damping time constant of ~14 ms for the resonance in vacuum, the authors conclude that a single ZnO nanowire can be used as a nanoresonator and a nanoscale cantilever. [25]

2.4.3 Sensor

ZnO nanostructures have been widely used for sensing applications because of their high sensitivity to the chemical environment. Because nanostructures have the advantage of a high surface area, and electronic processes are strongly influenced by surface processes. ZnO nanowires have demonstrated high sensitivity even at room temperature, whereas thin-film gas sensors often need to be operated at elevated temperatures.

The sensing process is governed by oxygen vacancies on the surface that influence the electronic properties of ZnO. Upon oxidation, via adsorption of molecules such as NO_2 at vacancy sites that accept electrons, electrons are withdrawn and effectively depleted from the conduction band, leading to a reduction

of conductivity. On the other hand, reducing molecules such as H_2 can react with surface-adsorbed oxygen, leaving behind an electron and a higher conductivity. The challenge is to sense certain gases selectively. [25]

Tien et al. developed a ZnO nanorod H_2 sensor. The sensitivity of their sensor was improved by sputter deposition of Pd clusters on the ZnO rod surface. The addition of Pd appears to be effective in the catalytic dissociation of H_2 into atomic hydrogen, increasing the sensitivity of the sensor device. The sensor detects hydrogen concentrations down to 10 ppm in N_2 at room temperature, whereas there is no response to O_2. By exposing the sensor to air or O_2, the conductance recovers to 95% after 20 s. [25]

2.4.4 Solar cell

Recently, nanostructured ZnO especially 1D ZnO structures are thought potential good electrode material for solar cell. The solar energy harvesting and conversion include three physical processes: (i) a light-absorbing material generates an electron-hole pair, (ii) the electron and hole separate quickly into two different phases, and (iii) the carriers are transported in these respective phases to opposing electrodes [27]. The dye-sensitized solar cell is one classic example of such photovoltaic device, in which light is absorbed by dye molecules adsorbed at the

interface between a network of TiO_2 nanoparticles and a hole conducting liquid electrolyte [28,29].

To further improve the solar energy conversion efficiency, using single-crystalline wide band gap semiconductor nanowires as the electron transport material instead of the mesoporous nanocrystalline TiO_2 film is considered a promising strategy. Because the nanowires can help improve electron transport by avoiding the particle-to-particle hopping that occurs in the TiO_2 network. Furthermore, the nanowire morphology can increase the likelihood that all photogenerated electrons have a direct connection to the collection electrode, without unnecessary lateral transport and the resulting recombination loss [27,30]. Therefore, the 1D ZnO structure seems very suitable candidate and has the advantage of easy controllable synthesis technology. Moreover, investigations have shown that ultra fast electron injection from the dye into the conduction band of the ZnO takes place, comparable to the timescale of electron injection into TiO_2 [31,32].

Chapter 3 Instrumentation

This chapter briefly describes the main equipments and techniques employed for the 1D ZnO nanostructures growth and characterizations.

3.1 Equipments for synthesis

3.1.1 Autoclave

Figure 3-1 [12] shows a schematic diagram of one mini-stainless steel autoclave and the Teflon liner usually used in the solution chemistry method. The lid of the Teflon cup is specially machined to ensure that tension will be applied to seal the cup when the metal cap is tightened. The separate Teflon liner fits snugly into the autoclave without leaving any gap.

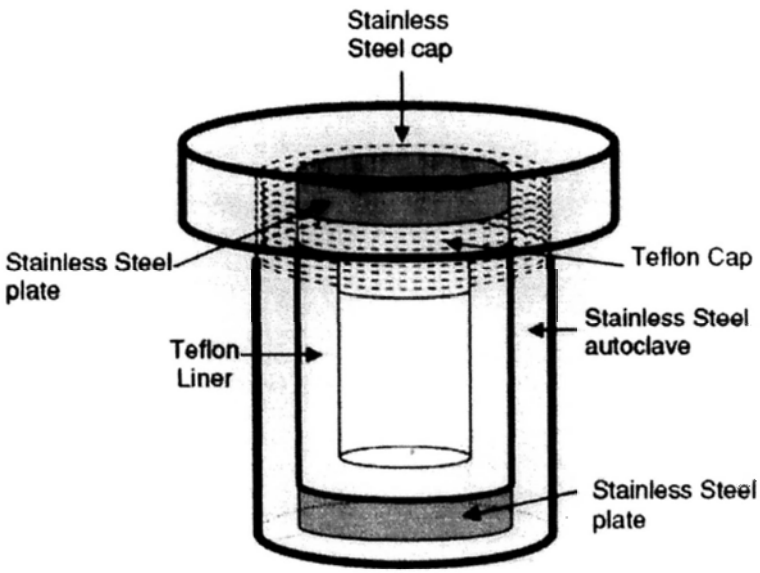

Figure 3- 1 Schematic diagram of one mini-stainless steel autoclave and its Teflon liner [12]

3.1.2 Vacuum tube furnace

Figure 3-2 is a schematic diagram of one vacuum tube furnace used in the evaporation method. The alumina tube (Φ40mm × 800mm) is inserted in a high temperature furnace. One end of the tube is connected to a vacuum pump and the other one to a gas flow controller then the gas cylinder. Source materials are usually located at the center and substrates the downstream of the tube. The base pressure in the tube can be pre-evacuated to less than 1×10^{-2} mbar, and the total pressure is maintained at 300 mbar during the synthesis by adjusting a needle valve located between one end of the tube and vacuum pump.

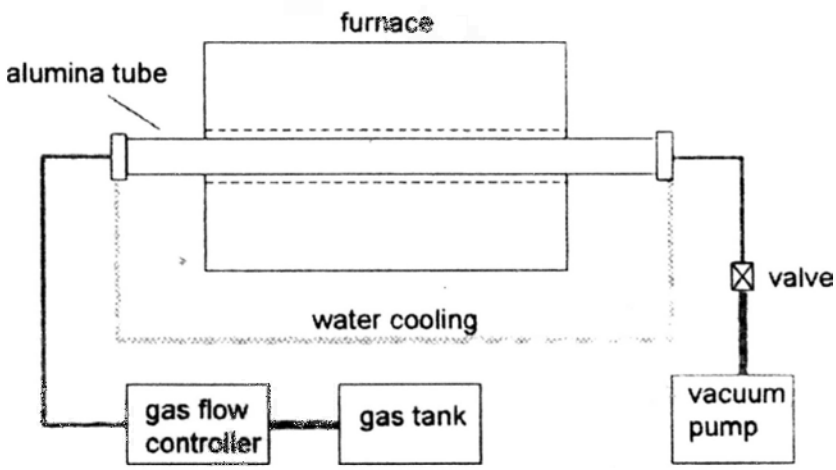

Figure 3- 2 Schematic of the vacuum tube furnace

3.2 Material characterization

3.2.1 Scanning Electron Microscope (SEM)

In a scanning electron microscope, electrons from a thermionic or filed-emission cathode are accelerated by a voltage of 1-50 kV between cathode and anode. Magnified by two- or three-stage electron lens system, an electron probe of diameter 1-10 nm with a current of $10^{-10} - 10^{-12}$ A is formed at the specimen surface. A deflection coil system in front of the last lens enables the electron probe to scan across the specimen. The subsequent signals from the specimen are then detected and recorded "point" by "point", corresponding to the location of the electron probe on the specimen [33].

A variety of electron-specimen interactions can be utilized to form an image and to generate qualitative and quantitative information. Part of the primary electrons are scattered from the specimen subsequently after the incidence. They are known as the Backscattered Electrons (BSE), which eject as a result of the multiple scattering(s). During the electron-specimen interaction, some loosely bound conduction electrons in the specimen are excited and ejected from the specimen surface, leading to the Secondary Electrons (SE) emission. Interaction with the energetic incident electrons can also ionize the tightly bound inner-shell electrons, leaving the atom in a highly energetic state. Subsequent de-excitation process

results in the emission of characteristic x-rays and Auger electrons. Specifically, an electron from an upper shell fills the vacancy in the ionized shell and release energy equating to $E_2 - E_1$ (E_2 and E_1 are the energy level of the upper and ionized shell, respectively). The released energy can be converted to an x-ray photon of energy $h\nu = E_2 - E_1$ or be transferred to another atomic electron, which leaves the specimen as an Auger electron with a characteristic kinetic energy of $E_2 - E_1 - \varphi$ (φ is the summation of the ionization energy of the leaving electron and the work function of the specimen).

The SE mode is the most useful one because the SE can be collected easily by means of a positively biased collector grid placed on one side of the specimen, thanks to their low exit energy of a few electronvolts. Behind the collector grid, the SE are accelerated onto a scintillator biased at + 10 kV and the light quanta generated are recorded by a photomultiplier. The dependence of the SE yield on the tilt angle of a surface element, the enhanced emission at edges and small particles, and the shadow contrast resulting from the incomplete collection, can be used to image the surface topography.

Most SEMs are equipped with an energy-dispersive lithium-drifted silicon detector, which allows characteristic x-ray lines to be recorded. Qualitative and quantitative x-ray analysis on the specimen can thus be processed.

In our experiments, a filed emission scanning electron microscope (FESEM QF400) attached with energy dispersive x-ray (EDX) is used to invest general morphology and composition of the products.

3.2.2 Transmission Electron Microscope (TEM)

A transmission electron microscope mainly consists of an electron gun, several sets of electronmagnetic lenses, and a data recording system [34]. Specimen is inserted in-between the second condenser lens and objective lens. In the electron gun, electrons ejecting from either a thermionic or filed-emission cathode are accelerated by a high voltage which can vary from 80 kV to 3 Mv. The accelerated electrons are then converged by the two sets of condenser lenses and irradiate the specimen. After scattering with the specimen, the transmitting electrons contain both structural and chemical information about the specimen. It is finally refracted and projected on to recording system by the objective lens, intermediate lens and projector lens. Both the electron diffraction pattern and the projected image of the specimen can be observed on the view screen. All of the corresponding specimen information can be recorded by either direct exposure of conventional photographic plate or a fluorescent screen coupled with a fiber-optic plate to a CCD camera digitally.

Signals can be generated during the interaction of the high-energy electron beam and a thin specimen. Most of these signals have been introduced in the SEM section. In TEM, due to the extremely high acceleration voltage, the electron transmission is greatly enhanced and strongly forward scattering becomes dominant compared to other scattering processes [35].

Electrons can be treated as particles, for which the electron scattering can be categorized into elastic and inelastic in nature, determined by whether the electrons have suffered from energy loss or not during the scattering process. When considering the electrons as wave, the terms of coherent and incoherent are commonly used, indicating their phase relations.

Electron Diffraction

If the incident electron beam is close to a zone axis of a single crystalline specimen, periodically arranged 2-dimensional spots will appear. These spots originate from the diffracted planes satisfying the Bragg's law, $2d\sin\theta_B = n\lambda$ (d is the distance between two adjoining atomic planes, θ_B is the angle between incident electron beam and the atomic planes, n is integral, and λ is wavelength of the incident electron beam). Polycrystalline specimens with random crystal orientations result in diffraction spots distributed randomly in the azimuthal direction. The diffraction pattern of an amorphous material consists of diffused rings, which are

caused by the short range atomic ordering in the specimen.

It is obvious that we can determine whether the specimen is crystalline just from the type of diffraction patterns observed (as stated above). Moreover, detailed analysis of the diffraction patterns can also provide us with the lattice symmetry and the inter-plane distance in the case of the crystalline specimen, and the nearest-neighbor structure in the case of amorphous specimens.

Contrast

The image contrast (C) can be quantitatively defined in terms of the difference in intensity (ΔI) between two adjacent areas

$$C = (I_2 - I_1)/I_1 = \Delta I/I_1$$

Several different kinds of contrasts are available in TEM images, which are illustrated in details in the following paragraphs.

(i)Mass-thickness Contrast

When electron beam transmits a specimen with non-uniform mass density or thickness distribution, it will be scattered to different extend in the different areas of the specimen. The thicker regions or those with larger mass will result in severer electron scatterings and larger scattering angles. Following this principle, mass-thickness contrast arises in the specimen image, reflecting the difference among different regions of the specimen in mass or thickness.

(ii)Diffraction Contrast

Diffraction contrast reflects the difference among different regions in crystal specimen in terms of satisfying the Bragg diffraction condition. We can create such contrast in TEM images by placing the objective aperture (diaphragm) covering the incident beam or any diffracted beam(s) to form Bright Field (BF) or Dark Field (DF) image. In order to obtain strong diffraction contrast in both BF and DF images, we could also tilt the specimen to a two-beam condition, in which only one diffracted beam is strong, and the direct beam is the other strong spot in the diffraction pattern. Such technique is extremely useful for the defect analysis in crystalline solid.

(iii)Phase Contrast

Contrast in TEM images can also arise due to the differences in the phase of the electron waves scattered by a thin specimen. High-Resolution TEM (HRTEM) image, in which the crystal lattice planes can be resolved, is a special case of phase contrast images. If the specimen is thin enough, it can be approximately considered that only the phase of electron wave is modified by the potential field of the atoms in the specimen, while the amplitude of the electron wave remains constant. As the electron wave transmits through the specimen, additional phase shift that depends on scattering angle, the spherical-aberration constant C_s and the defocusing Δz is added on due to the imperfection of the lens system. The finally phase contrast in the

image is formed by the interference of many electron waves. It is determined by both the potential field of the specimen and the imperfections of the lens system. However, under the proper defocus condition (known as the Schetzer defocus), the contrast will reflect the potential field directly and thus the atomic arrangement of the specimen.

X-ray Microanalysis

As characteristic x-rays generated during the electron-specimen scattering, equipped with x-ray detector and spectrometer TEM can do x-ray analysis of the specimen as well. Moreover, x-ray production in thin specimens is confined to the small volume excited by the small electron probe, thus better spatial resolution is achieved.

Energy-loss Spectrum

When the electron beam traverses a thin specimen, it loses energy by a variety of processes. The resulted inelastically scattered electrons can be dispersed by a Electron Energy-Loss Spectrometer (EELS) and thus the information they contain be quantified.

There are three principal regions of an energy-loss spectrum: (1) The zero-loss peak, which consist primarily of elastically forward-scattered electrons, but with a small portion of electrons that have suffered phonon losses. (2) The low-loss region

up to an energy loss of ~50 eV contains electrons, which have interacted with the weakly bound outer-shell electrons of the atoms in the specimen. (3) Electrons in the high-loss region have interacted with the more tightly bound inner-shell or "core" electrons. These different regimes of energy losses can give us different information about the specimen. The zero-loss peak defines the equipment energy resolution and is essential in calibrating the spectrum. The electrons in the low-loss region have interacted with outer-shell electrons (valence electrons) in the specimen, so that contain information about the electronic structure near the Fermi level. The electrons in the high-loss region have "probed" the inner electron shells and therefore contain information characteristic of the element(s) in the specimen.

A 200 kV accelerated field emission transmission electron microscope (Tecnai 20ST FEG), which is equipped with EDX and EELS systems was employed in our experiments.

3.2.3 X-Ray Diffraction (XRD)

The principle of the powder x-ray diffraction method is illustrated by the diagrams of Fig. 3-3 [36]. Figure 3-3a shows a particular set of lattice planes in one crystalline oriented at the appropriate Bragg angle θ to the incident beam. The reflected beam makes an angle 2θ (the diffraction angle) with the undeviated beam.

The figure depicts only one of an infinite number of ways in which this, or an identical set of planes in another crystallite, can be oriented at the same angle θ to the beam. The reflected beams which correspond to these orientations outline a cone, which is coaxial with the incident beam and has a half-apex angle 2θ (Fig. 3-3b). Simultaneously, other lattice planes with different spacing satisfy the Bragg condition and generate reflection cones, which are also coaxial with the beam but have different half-apex angles (Fig. 3-3c). Reflections developed at 2θ angles of less than 90° are described as front or forward reflections and at angles greater than 90° as back reflections. Reflections are recorded on film or are detected by a radiation counter which will actuate a pen on a strip-chart to produce a graphical record. This apparatus is known as an x-ray diffractometer.

The characteristic features of an x-ray powder spectrum are the angles at which reflections occur and the relative intensities of the reflections. The reflection angles θ depend on the wavelength λ and the interplanar spacing d_{hkl} in accordance with the Bragg law $\lambda = 2d_{hkl}\sin\theta$. The spacing in turn depends on the dimensions of the unit cell.

A Rigaku, Philips, Huber (RU-300, MRD, V612365) x-ray diffractometer was used to provide information on the crystallinity of the specimens.

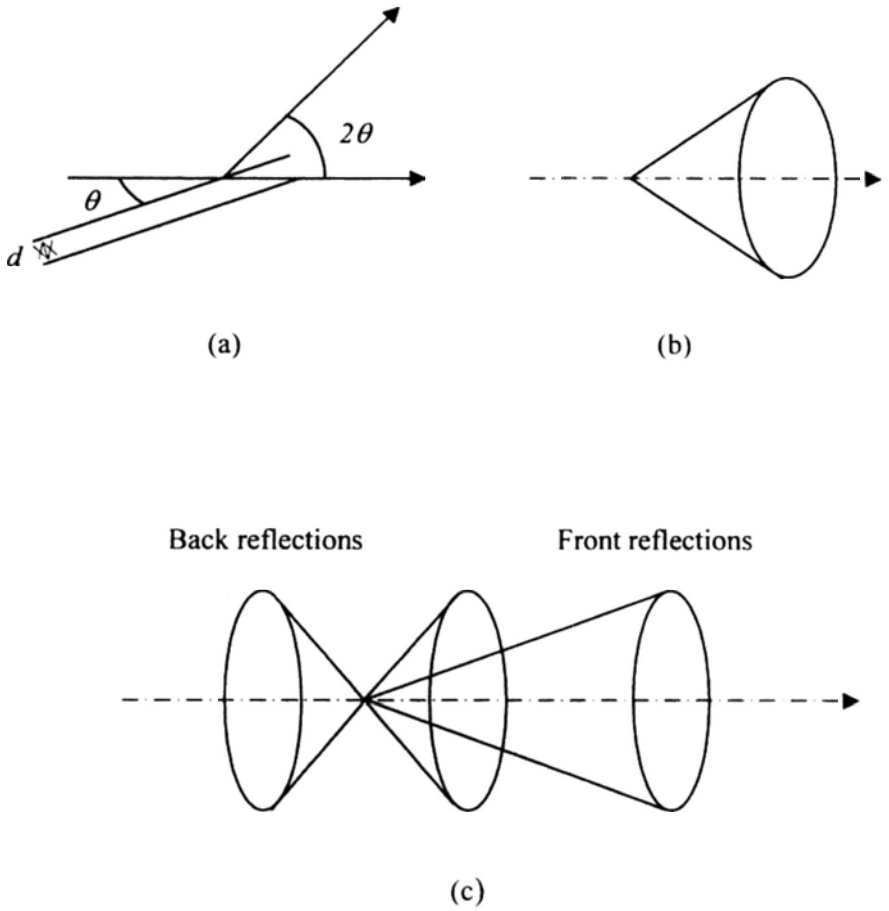

Figure 3- 3 The principle of the powder XRD method [36]

3.2.4 Cathodoluminescence (CL) measurement

Cathodoluminescence is the emission of light resulting from the electron bombardment process. In an electron probe instrument, electron irradiation of a solid results in a variety of useful signals. Some primary electrons, absorbed in the bulk of the material, will dissipate their energy in various electronic excitations. The generation of electron-hole pairs may lead to the emission of photons in the ultraviolet, visible, and infrared spectral ranges, i.e., cathodoluminescence [37].

Cathodoluminescence and other luminescence phenomena, such as

photoluminescence (PL), yield similar results with some possible differences associated with the details of the excitation of electron-hole pairs, for example in the generation rate and excitation volume. Electron beam excitation in general leads to emission by all the luminescence mechanisms present in the semiconductor. An advantage of CL, in addition to the high spatial resolution, is its ability to obtain more detailed depth-resolved information by varying the electron beam energy.

A Cambridge S-360 Scanning Electron Microscope (SEM), which is implemented with Oxford cathodoluminescence instrument and a charge-coupled detector (CCD), is employed to taken the emission spectra. The accelerating voltage of the electron beam is 10 kV. All the spectra were taken at room temperature.

2.2.3 Optical extinction measurement

Absorption spectra of the specimens were recorded using a UV-350 spectrometer. The samples were attached to a metal plate containing holes with double face adhesive tape. They were illuminated from the glass side.

Optical absorption is expressed in terms of the absorption coefficient , defined by Lambert's law [37]

$$I = I_0 \exp(-\alpha x)$$

for the radiation intensity I falling off with distance x through the sample. For direct transitions between parabolic conduction and valence bands, the absorption coefficient is described by

$$\alpha(h\nu) = A(h\nu - E_g)^{1/2}$$

where hν is the photon energy, E_g stands for band gap value of the corresponding semiconductor, and A is a constant. By plotting $(\alpha h\nu)^2$ versus $h\nu$, and extrapolating the straight portion of the plot to the energy axis at $\alpha=0$, we can estimate the band gap value for the specimen.

Chapter 4 A Simple Route to Controllable Growth of ZnO Nanorod Arrays on Zn foil

In this chapter, we have employed a simple and low cost method to grow aligned ZnO nanorod arrays on Zn foil. The average diameters of the nanorods can be tuned from ~20 nm to ~150 nm by varying the growth conditions. Optical property of these nanorods has been studied and discussed by correlating them to the structural quality of the nanorods.

4.1 Experiment

A general procedure to synthesize ZnO nanorod arraysof ZnO nanorod can be found in the following: A mixture of 10 mL NaOH and 5mL H_2O_2 aqueous solution is firstly added in a 20 mL stainless steel Teflon-lined autoclave. A piece of 2 cm × 2.5 cm zinc foil is then added to the above solution before the autoclave is sealed. The autoclave is then kept at a constant temperature for several hours before the system return to room temperature. At last the zinc foil is taken out from the solution, rinsed with distilled water and dried in air. We have identified three synthesis parameters that would affect the morphology and structural quality of the ZnO nanorod arrays, i.e. the concentration of H_2O_2 and NaOH in the solution and their relative ratio, as well as growth temperature.

4.2 Results

Figure 4-1 shows the SEM images of the samples synthesized with different solution composition but at the same temperature (150℃) and for the same duration (2h). Three different solution composition has been used, i.e., (a) 5 mL 1% H_2O_2 and 10 mL 2M NaOH, (b) 5 mL 0.5% H_2O_2 and 10 mL 2M NaOH , (c) 5 mL 0.25% H_2O_2 and 10 mL 2M NaOH. Thick nanorods are obtained for both (a) and (b) with a large non-uniformity existing in the nanowire diameters. These nanorods are composed of O and Zn, as suggested by the EDX analysis (Figure 4-2a). XRD spectra taken from these specimens reveal the wurtzite structure of the nanorod (Figure 4-2b). A slight decrease in the average diameter of these nanorods is observed when the H_2O_2 concentration is reduced from 1% to 0.5%. Nevertheless, when the H_2O_2 concentration is further reduced to 0.25% and below, no obvious nanorod growth is observed on the Zn foil. Instead, a rough surface (Figure 4-1c) composed of Zn and a small amount of O is found. On the other hand, the morphology of the product is also affected by the concentration ratio of H_2O_2 and NaOH. As we reduce the concentration of NaOH solution to 0.2M, but keeping H_2O_2 concentration at 0.25%, nanorods start to grow on the Zn foil surface again (Figure 4-3). At the same time, uniformity of the nanorods has been improved, with an average diameter being reduced to ~ 70 nm.

Temperature is another important factor in tuning the nanorod diameter. In the temperature series, we have fixed the reaction temperature at ~150℃, ~70℃, ~21℃, and ~5℃, respectively. (The solution consists of 5mL 0.5% H_2O_2 and 10mL 0.2M NaOH). We found that the diameter of the ZnO nanorods decreases dramatically with the decreasing of synthesis temperature. At 70℃, the average diameter of the nanorods is ~30 nm (Figure 4-4b). When the synthesis temperature goes down to 21℃, average diameter of the ZnO nanorods is further reduced to around ~20 nm. Nevertheless, further reducing the temperature to 5℃ fails to result in ZnO nanorod of any smaller diameters. Figure 4-5 shows the TEM images taken at the nanorods with small diameters. Each nanorod is single crystalline, with wurzite ZnO [0001] as the growth direction. However, the narrower nanorods are more subjective to electron beam irradiation damaged in the TEM. More and more small regions with brighter contrast as indicated by arrows in the high resolution image appear with the increasing of electron beam illumination time. It is caused by the electron beam sputtering and thinning effect on the specimen [38].

Figure 4-6a and 4-6b show typical cathodoluminescence (CL) spectra taken from ZnO nanorods with average diameter of 120 nm and 30 nm, respectively. Strong band edge emission is always observed when the diameter of the ZnO nanorod is large (≥70 nm). While for nanorods with smaller diameters, band edge

emission becomes weak and defect emission dominates in the spectra. The defect emission from the thin nanorods covers a wide wavelength range starting from 450 nm to 800 nm, with maximum at ~ 600 nm. A similar broad defect emission but with very low intensity centered at ~560 nm can also be observed from the wide nanorods. The yellow and orange emissions are normally assigned to O interstitial or the presence of -OH group; while the green emission may result from Zn vacancy, and O vacancy etc., the origin of which remains controversial [17,18]. The broad non-UV luminescence peak from the specimen indicates that more than one type of defects are involved.

4. 3 Discussion

4.3.1 General growth mechanism of the ZnO nanorod arrays

The growth mechanism of the ZnO nanorod arrays on the Zn foil has been discussed in our previous study [39]. Briefly, H_2O_2 serves as a strong oxidant for the Zn foil in the alkaline solution of NaOH. The Zn foil would be readily oxidized starting with a large amount of ZnO nanoclusters on the foil surface. This is revealed by the SEM image (Figure 4-7a) taken at initial stage of the nanorod growth. Occasionally, through a sparsely packed nanorod array, small particles with diameter around 5nm can still be observed on the substrate (Figure 4-7b). These

nanoclusters become the nuclei for further ZnO crystal growth as the oxidation proceeds. With ZnO's natural tendency of anisotropic growth along the crystalline *c* axis ([0001] crystalline direction), the produced strong oxidizing environment serves as a kinetic driving force and promotes the anisotropic development and thus the growth of elongated nanocrystals. As a result, ZnO nanorod arrays on the Zn substrate are formed with all of the nanorods growing along the crystalline *c* axis.

4.3.2 Appropriate concentration ratio between H_2O_2 and NaOH for the nanorod growth

Concentration (or mass) ratio between H_2O_2 and NaOH determines the composition and morphology of the final product. If the ratio is too high (for example, ≥5%/0.2M), the Zn foil is passivated, with a completely oxidized surface formed soon after the reaction starts. When such a compact ZnO layer immediately forms on surface of the Zn foil, it slows down the further oxidation process of the Zn. More importantly, the ZnO nucleus would fail to form, and thus no further 1D growth. If the H_2O_2/NaOH ratio is too low (for example, 0.25%/2M), all of the ZnO forming due to oxidation would dissolve in the strong alkaline solution faster than the further formation of ZnO ($ZnO + H_2O + 2OH^- \rightarrow Zn(OH)_4^{2-}$) [40], leaving an etched Zn surface.

ZnO nanorod arrays only appear at a medium concentration (or mass) ratio between H_2O_2 and NaOH. Under such condition, the ZnO seed layer initially forms on Zn foil surface is not compact allowing further oxidation of Zn to occur and contribute to the ZnO nanorod growth. The appropriate concentration ratio between H_2O_2 and NaOH for ZnO nanorod arrays growth approximately ranges in 2.5 ~ 0.25 (%/M).

4.3.3 Average diameter of the ZnO nanorods

Diameter of the ZnO nanorods varies with two factors, i.e. the concentration of the H_2O_2 solution and the synthesis temperature. High H_2O_2 concentration (for example 1%) produces a great amount of source material in the solution, which allows the nuclei continuously increase their volumes and form nanorods with large average diameter (~150nm). As the concentration of the H_2O_2 solution decreases, supply of the source material that contributes to ZnO nanorod growth is reduced. It will restrict the augment of the nanorods in both their diameter and length.

Growth rate of the nanorods highly depends on the synthesis temperature. Lowering the temperature effectively slows down the crystal growth process, which makes the products keep at smaller size in both their lateral and longitudinal aspects, as the synthesis process is terminated after a certain period of time.

4.3.4 Uniformity of the ZnO nanorod arrays

Uniformity of the ZnO nanorod arrays is simultaneously affected by the concentration ratio of H_2O_2 to NaOH, the synthesis temperature, as well as surface roughness of the substrate. A higher concentration ratio of H_2O_2 to NaOH (for example, ≥1.25%/M) helps to form nanorod arrays with better uniformity. This is because adequate source material is supplied during the nucleation and growth processes of the nanocrystals, which makes the existing seeds on the Zn foil surface grow at similar rate. While the H_2O_2 to NaOH concentration ratio decreases, supply of the source material is limited. It creates local difference on the amount of the source material, which could be increased due to the surface roughness of the Zn foil and/or accelerated dissolving rates at grain boundaries on the foil surface. As a result, the existing seeds on the foil surface grow at different rates, forming nanorods with various diameters. Moreover, as time increases, small sized nanorods may start to dissolve in the solution again and re-grow onto those undissolved larger ones—a mechanism similar to Ostwald ripening [41]. This makes the sizes of tiny crystals reduce while the larger ones increase, further deteriorating the nonuniformity of the nanorod arrays.

For a specified H_2O_2/NaOH ratio, there is a temperature range that makes the

nanorod arrays have better uniformity, e.g. for 1.25%/M, the temperature range ≤70℃ is appropriate. Once the temperature gets too high, the ZnO solubility in the solution is dramatically increased [42], which equals to a large reduction on the supply of the source material.

At lower temperature (≤70℃), surface roughness of the Zn foil also becomes a dominant factor that determines the uniformity of the nanorod arrays. With the decreasing of temperature, reactions and diffusion in the solution gradually slow down. The local concentration difference of the source material is more easily to be produced on a rough substrate surface, worsening the uniformity of the nanorod arrays. Indeed, flattening the Zn foil surface by electro polish or mechanical polish is proved to improve uniformity of the nanorod arrays (Figure 4-8).

4.3.5 Different luminescence properties for nanorods with different diameter

The larger-diametered nanorods are grown under higher temperature (150℃). In addition, the concentration of the oxidant—H_2O_2 is relatively higher for the larger-diametered nanorod growth. The more abundant oxidation source and the higher temperature help to reduce the native point defect formation in the ZnO nanorods, and lead to their improved electronic structure quality. This explains the much stronger band edge emission and weaker defect emission (mainly from

intrinsic defects) in the larger diametered nanorods. In addition, the surface to volume ratio is also significantly increases in the smaller-diametered nanorods, when surface defect luminescence could also make a contribution [17].

4.4 Conclusions

ZnO nanorod arrays on conducting substrates are demonstrated using a solution chemistry approach. The nanorod arrays are uniformly distributed on entire surface of the foil. By systematically varying the synthesis temperature, the relative concentrations of H_2O_2 and NaOH, we found that the average diameter of the ZnO nanorods can be tuned from ~150 nm to less than 20 nm. Larger-diametered nanorods are found to possess higher band edge to defect emission ratio, indicating their better electronic structural quality, which is determined by both the growth conditions and the nanorod surface-to-volume ratio.

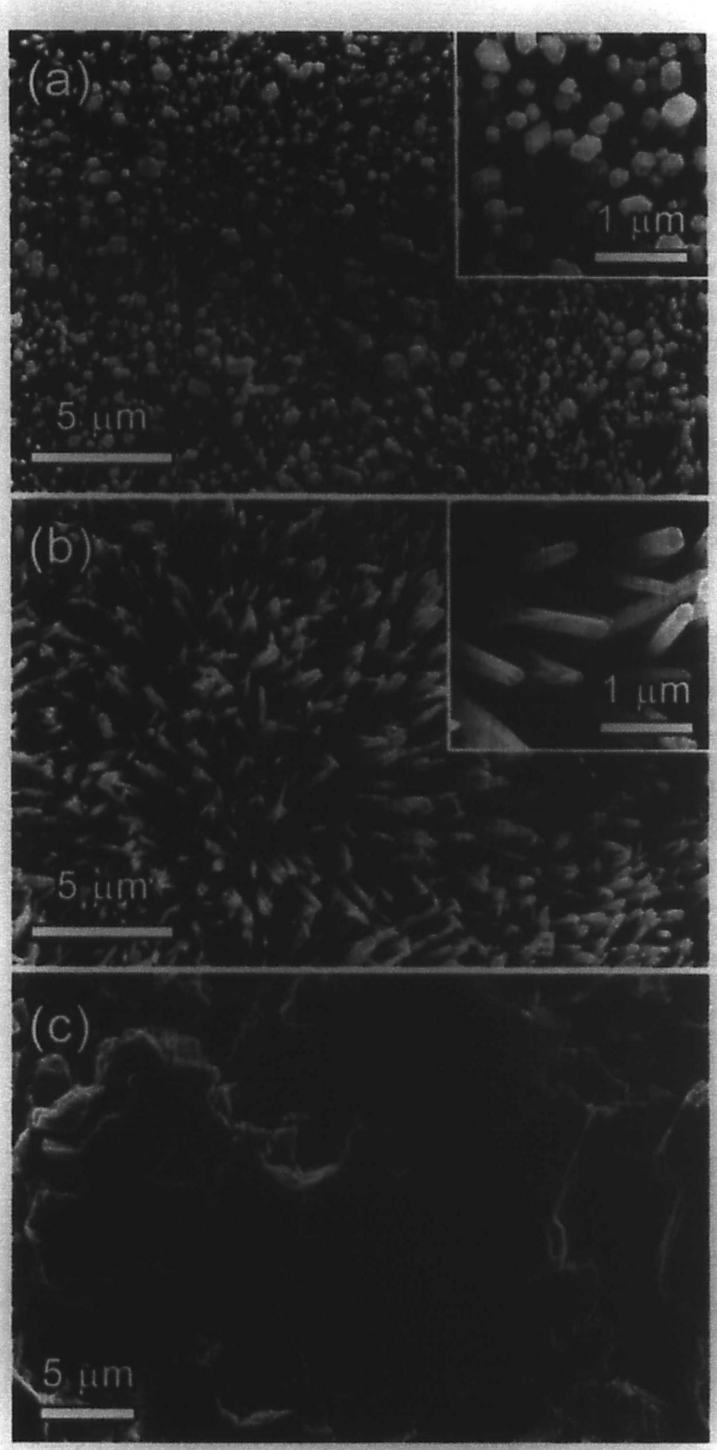

Figure 4- 1 SEM images of samples synthesized in mixed aqueous solution of (a) 5 mL 1% H_2O_2 and 10 mL 2M NaOH (b) 5 mL 0.5% H_2O_2 and 10 mL 2M NaOH (c) 5 mL 0.25% H_2O_2 and 10 mL 2M NaOH. All solutions were kept at 150℃ for 2h.

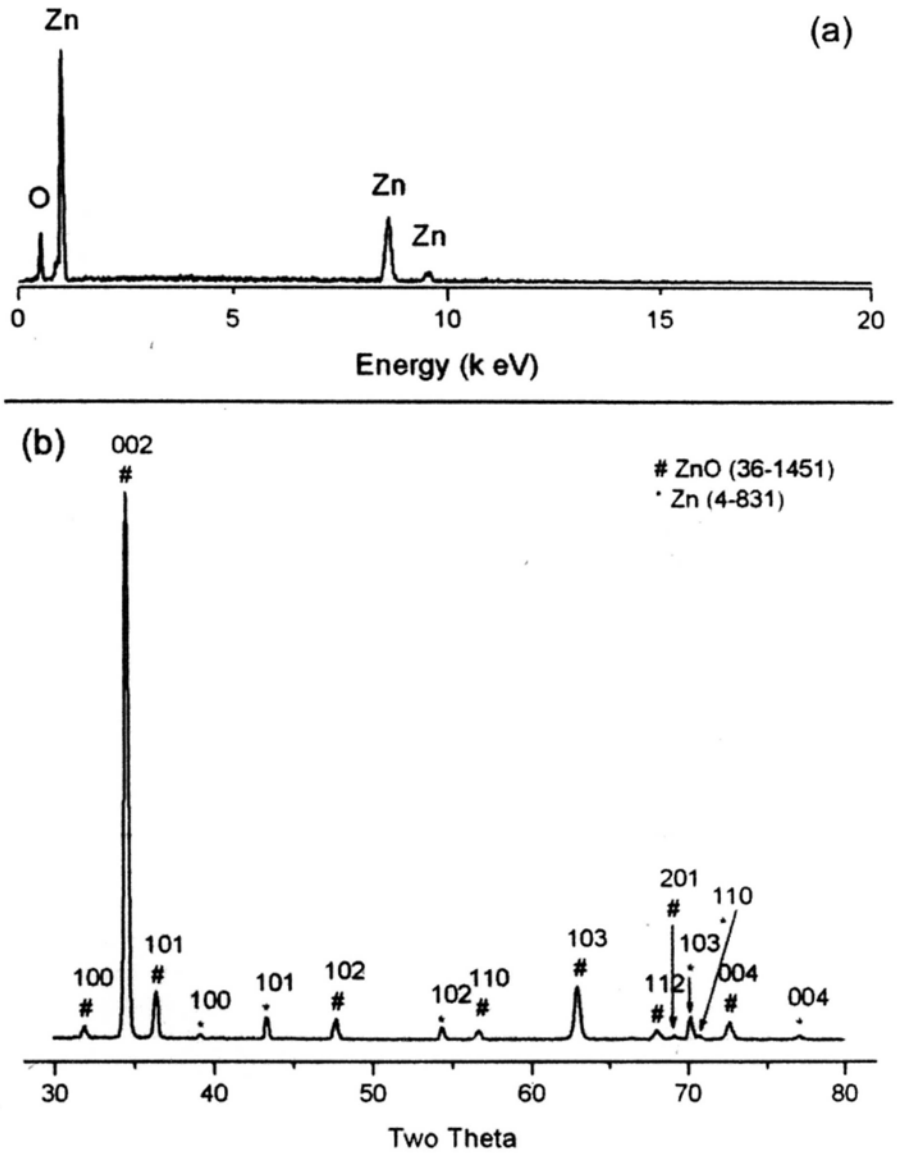

Figure 4- 2 (a) EDX spectrum taken from thick ZnO nanowires on Zn foil; (b) XRD spectrum taken from thick ZnO nanowires on Zn foil.

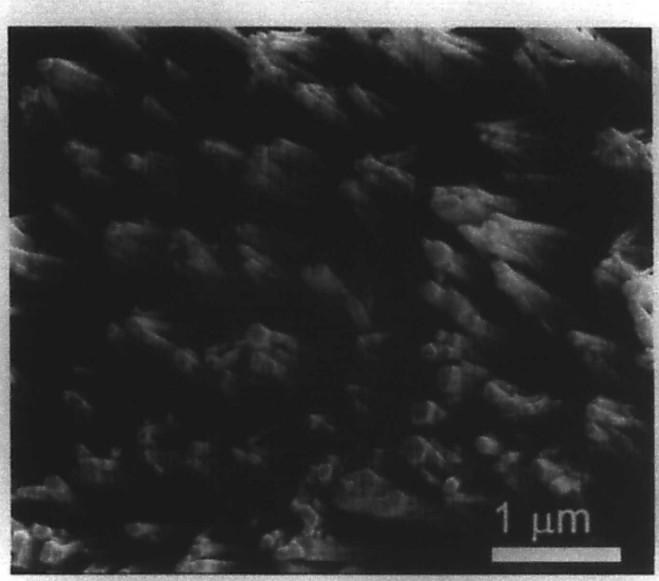

Figure 4- 3 SEM image of specimen synthesized at 150℃ for 2h, with the mixed aqueous solution of 5 mL 0.25% H_2O_2 and 10 mL 0.2M NaOH.

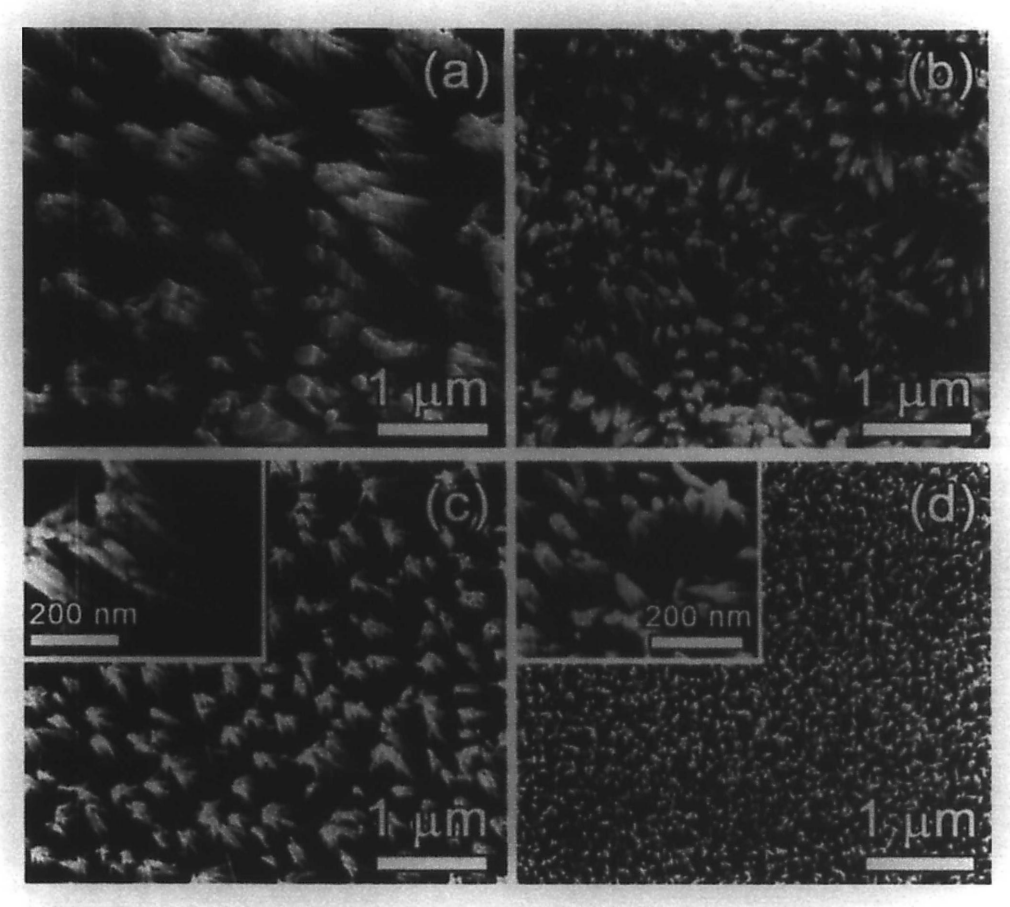

Figure 4- 4 SEM images of samples synthesized at (a) 150℃ (b) 70℃ (c) 21℃ and (d) 5 ℃ with aqueous solution of 5mL 0.25% H_2O_2 and 10mL 0.2M NaOH. Insects are larger magnification pictures of the sample.

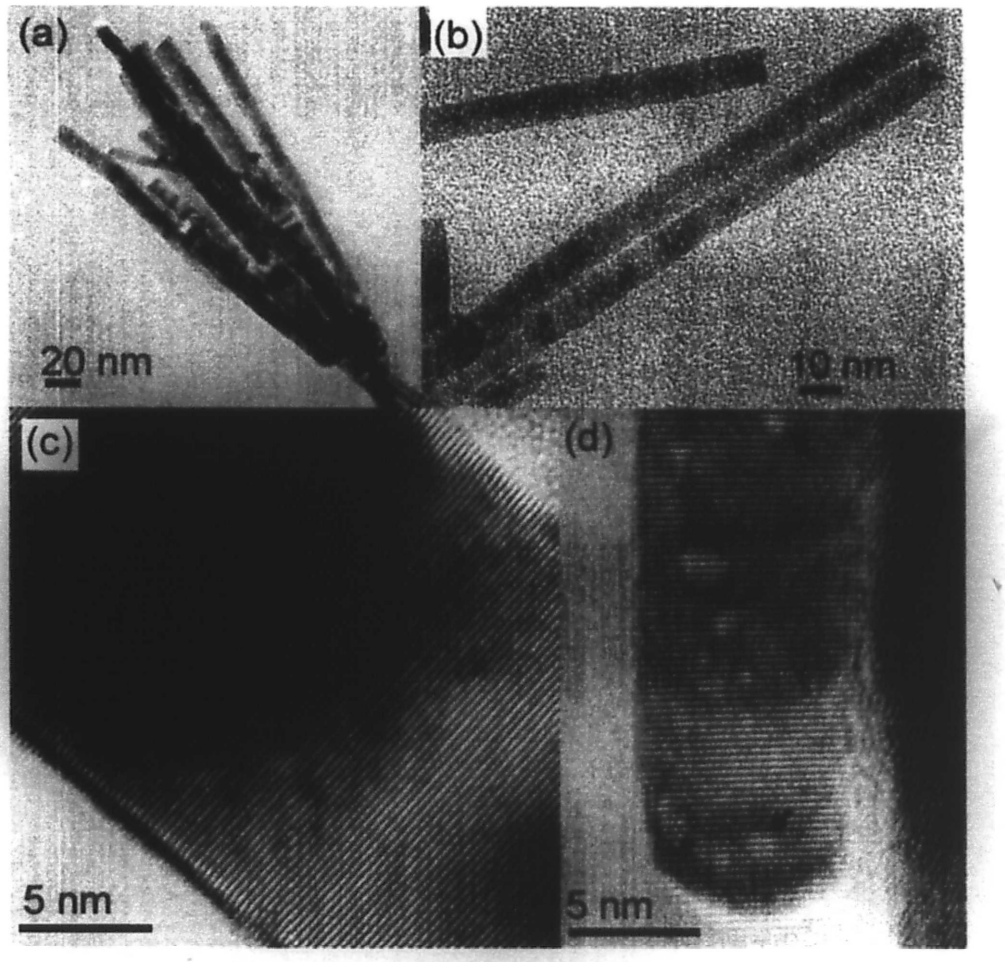

Figure 4- 5 (a), (b) low magnification TEM images taken on ZnO nanowires with diameter of 16nm and 10 nm. (c), (d) high resolution TEM images taken on ZnO nanowires with diameter of 16 nm and 8nm. Arrows in (d) point damaged regions on the specimen, which are induced by electron beam irradiation during the observation.

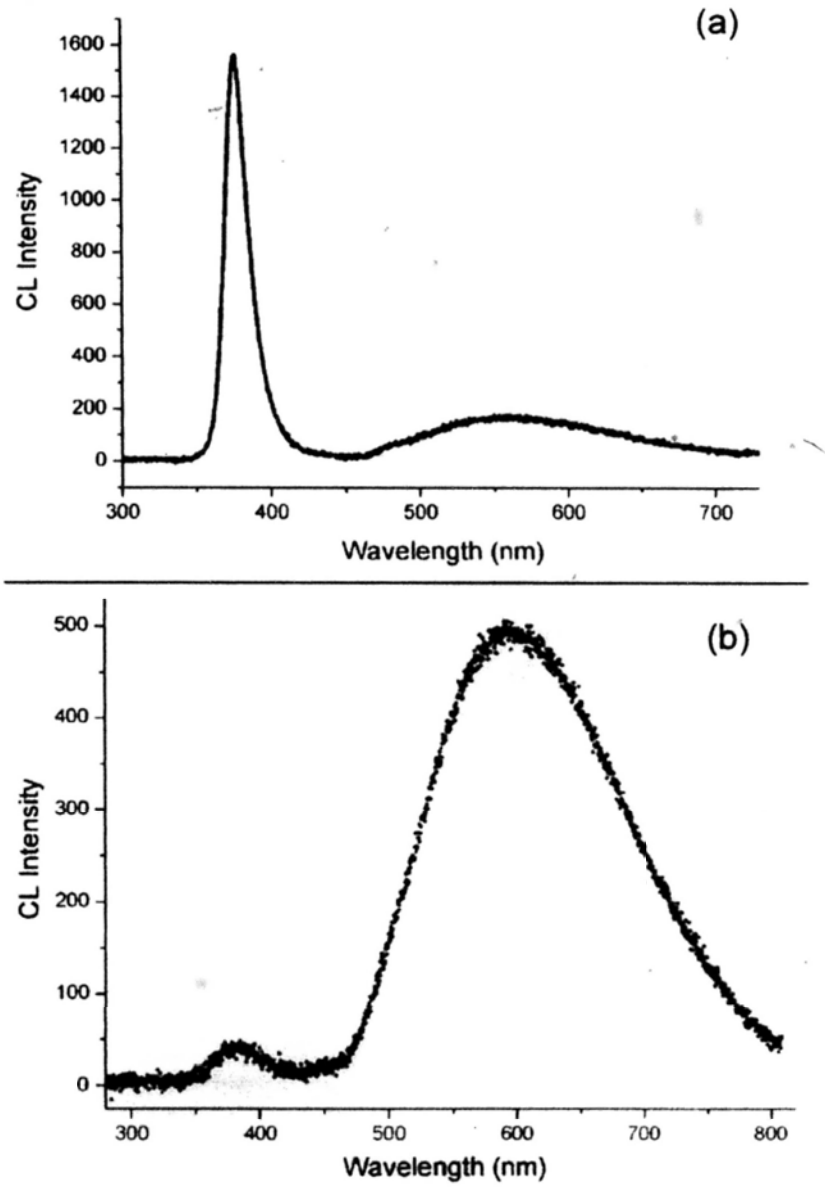

Figure 4- 6 Room temperature cathode luminescence spectra taken from the ZnO nanowires with average diameter around (a) 120 nm and (b) 30 nm.

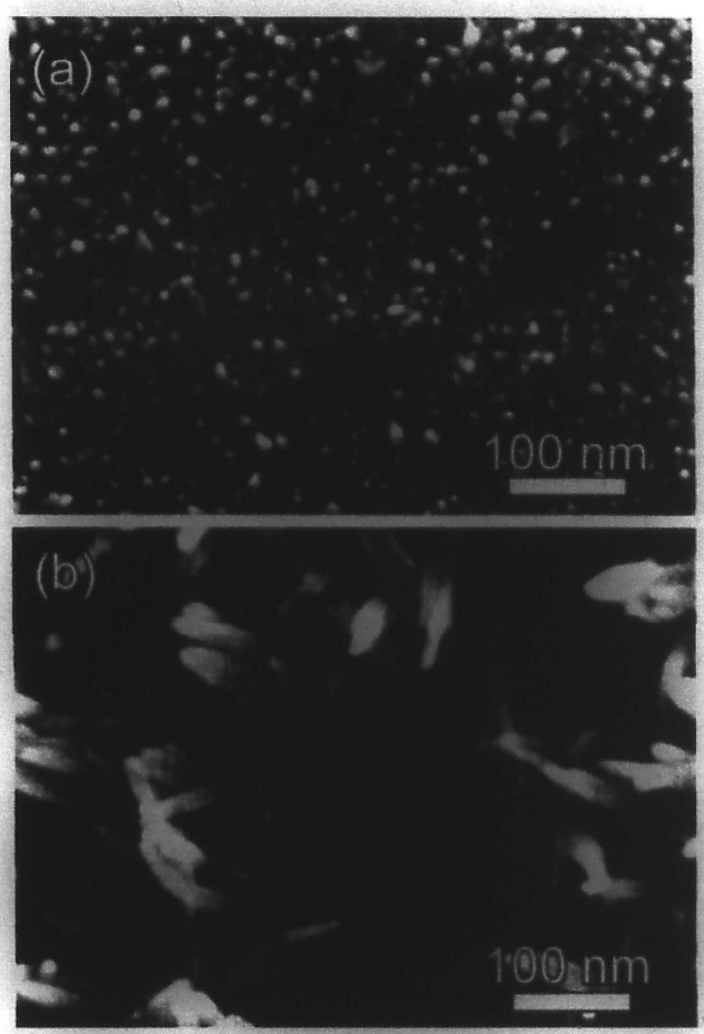

Figure 4- 7 (a) SEM image taken at the initial growth stage of the specimen prepared at 21℃ with aqueous solution of 5mL 0.5% H_2O_2 and 10mL 0.2M NaOH. Nanoclusters with diameter around 5nm cover on the Zn foil surface. (b) Occasionally, through a sparsely packed nanorod array, some nanoclusters on the substrate can still be observed by SEM. The nanorod was prepared at 40℃ with aqueous solution of 5mL 0.25% H_2O_2 and 10mL 0.2M NaOH.

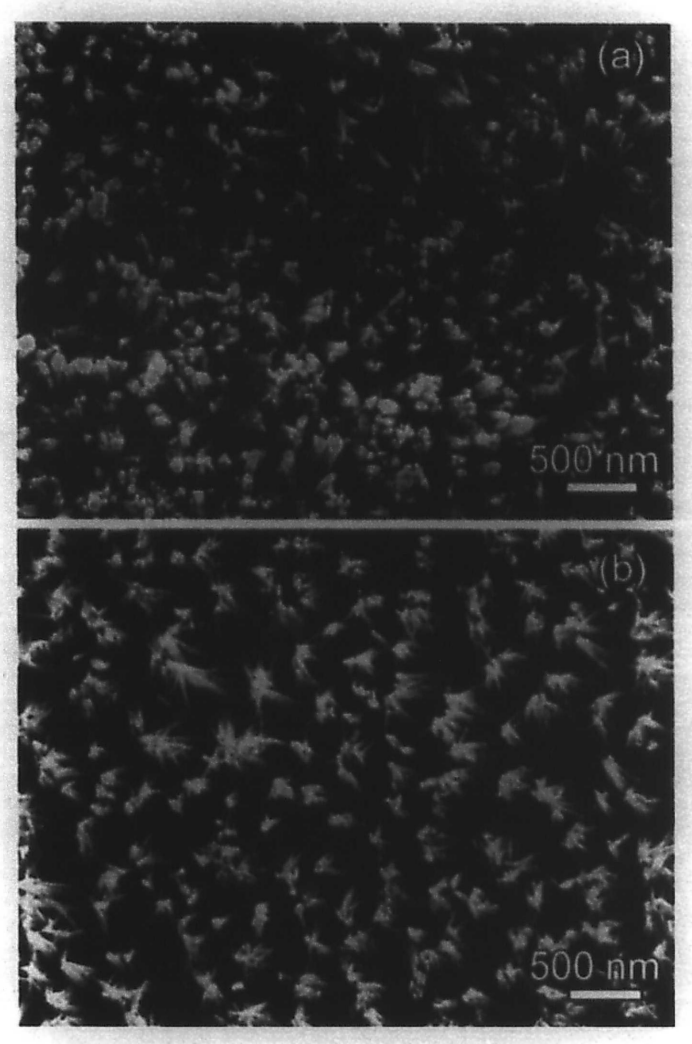

Figure 4- 8 SEM images of nanorod arrays prepared on (a) as purchased Zn foil, and (b) electro polished Zn foil. Other synthesis conditions for the nanorod arrays were kept same, i.e. 21℃, with mixed aqueous solution of 5mL 0.25% H_2O_2 and 10mL 0.2M NaOH. The nanorod array on polished Zn foil has better uniformity.

Chapter 5 Controllable Growth of ZnO Nanorod Arrays by Thermal Evaporation Method

In the last chapter we have investigated controllable growth of ZnO nanorod arrays using a solution-based method. In this chapter, we present a series studies on a vapor phase transport deposition of ZnO nanorod arrays. Effects of several growth parameters, including the base vacuum pressure, oxygen gas supply and an additional small quartz tube in the original vacuum tube furnace setting, on the morphology, structural quality and properties of the products are studied.

5.1 Experiment

A general procedure for the synthesis can be found in the following: A high temperature vacuum tube furnace is employed for the processing. ZnO and graphite powders with mass ratio 3:1 were mixed and placed at center of the alumina tube in the furnace as the starting material. Pieces of silicon wafer were placed at downstream of the tube. The tube was then sealed and pumped to a base vacuum pressure. Carrier gas (pure Ar) was introduced into the tube at a constant flow rate of 80 sccm, after which the total pressure of the system was kept at 300 mbar for the whole fabrication process. The tube was heated up to 1100℃ and maintained at the same temperature for 30 min.—1h. After the tube was cooled down to room temperature, the silicon wafers were collected at the downstream of the tube for

further study.

By deliberately leaking air into the sealed system, the base vacuum pressure can be controlled. We firstly study effect of different vacuum base pressures on morphology of the products. The base pressures employed in the present study are list in Table 5-1. We also found another two synthesis conditions could affect the growth of the products. One is presence/absence of pure oxygen in the system after temperature reached 1100℃. The other is the adoption of a small quartz tube in the tube furnace with the source powder and silicon substrates loaded into the small quartz tube. A schematic of such setting can be found in the following (Figure 5-1).

Table 5- 1 Tested Base Vacuum Pressures (Torr)

8×10^{-3}	3.5×10^{-2}	7×10^{-2}	1×10^{-1}

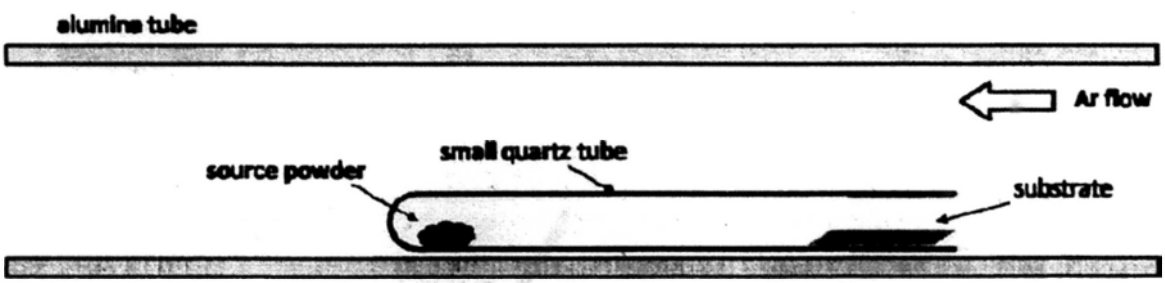

Figure 5- 1 Schematics of the set up with a small quartz tube

5.2 Results

5.2.1 General morphology of ZnO products synthesized at different conditions

Figure 5-2 shows the typical morphologies of the products grown under increasing vacuum base pressures. When the vacuum base pressure is too low (8×10^{-3} Torr), little product is found on the substrate surface (Figure 5-2a). A vacuum base pressure at ~ 3.5×10^{-2} Torr leads to nanorod array growth. These nanorods have rather uniform diameter (~ 40 nm) and aspect ratio around 10 (Figure 5-2b). When the vacuum base pressure is increased to 7×10^{-2} Torr, rod-like particles are found to be distributed on the substrate, with aspect ratio around 2~5. The diameters of those particles become larger than 100 nm, with a rather large size fluctuation. Further increase the vacuum base pressure to 1×10^{-1} Torr results in a rough film growth, comsisting of many irregular particles (Figure 5-2d).

Figure 5-3 shows several SEM images taken from the specimen synthesized at 3.5×10^{-2} Torr base pressure. One will notice that in some regions on the substrate, the nanorods are vertically aligned, like shown in Figure 5-3a. An enlarged top view of a vertically standing nanorod (inset in Figure 5-3a) reveals its hexagonal cross section. However, observation on larger scale reveals that the coverage of the nanorod arrays on substrate is not ideal, as patches of undeposited regions exist (Figure 5-3b). Areas covered by nanorods with similar density only last for tens of

microns square or slightly larger. This is a drawback for this simple synthesis approach once large area nanorod arrays are demanded.

When oxygen is deliberately introduced during the nanorods growth, there is an obvious improvement on the substrate coverage uniformity. Both the density of the nanorods and the amount of vertically aligned nanorods are found to be increased (Figure 5-4a). The area covered by nanorod arrays (Figure 5-4a) can be extended to larger than hundreds of microns square. Figure 5-4d is partially cut from a lower magnification SEM image taken on a typical area. Nevertheless, orientation distribution of the nanorods in arrays still exists. Both the Length and diameter of the nanorods also increase under such a growth condition. Figure 5-4b and 5-4c demonstrate the typical nanorods longer than 500 nm and with diameter around 70 nm.

With the assistance of a small quartz tube, the yield of the nanorod arrays is found to be significantly improved. Full coverage of the substrate surface (~ $1cm^2$) is achieved. The morphology of the arrays deposited on different temperature zones are found to vary, as shown in Figure 5-5a to 5-5d. Nanorods with diameter of 200 nm and length of 2 μm grow on the highest temperature zone (~630℃). However, density of the nanorods is rather low, and the orientations of the nanorods are disordered. In a lower temperature zone, the density of the nanorods is found to

increase, together with improvement on the vertical alignment of the nanorods. At the same time, both the diameter and the length of the nanorods further increase. Figure 5-5e is a low magnification SEM image taken on the vertically aligned nanorod arrays, showing its large area and uniformity.

5.2.2 TEM characterizations of the nanorods

Figure 5-6 shows the typical TEM characteriations of the specimens. Low magnification TEM image (Figure 5-6a) demonstrates the rod morphology, which is consistent with SEM observation. The high resolution (HR) TEM image reveals the single crystallinity of individual nanorod. Figure 5-6b is a typical HR image of hexagonal ZnO nanorod taken from the [01-10] zone axis, disclosing its growth direction along the ZnO crystalline [0001] direction. EDX spectrum (Figure 5-6c) taken on the specimen further confirms its composition of Zn and O.

5.2.3 Cathodoluminescence properties of the ZnO nanorod arrays

Room temperature cathodoluminescence spectra of the nanorod arrays synthesized at the three different conditions are shown in Figure 5-7 and 5-8. For the first two cases (base pressure of 3.5×10^{-2}Torr, w/o oxygen presence during the nanorod array growth), defect emission centered at ~ 520 nm dominates the CL

spectrum, although the ZnO band edge emission at ~380 nm is also observed. When the additional small quartz tube is introduced into the setting, the CL property of the specimen is found to depend on the temperature of the sample depositing zone. In the high temperature zone, the ZnO nanorods possess a strong band edge emission and a lower defect emission at ~ 520 nm. Decreasing the substrate temperature (low temperature zones) leads to the suppression of the ZnO band edge emission and enhancement of the defect emission with the defect emission peak center remains at ~520 nm. For specimen grown at the lowest temperature zone, not only the ZnO band edge to defect emission ratio is further reduced, but the center of defect emission shifts to ~ 620 nm, suggesting change in the defect state in the sample.

5.3 Discussion

5.3.1 General growth mechanism of the ZnO nanorod arrays

Previous study has shown that ZnO nanostructures can directly form from vapor phase without the assistance of metal catalyst. Since we did not use any catalyst on the substrate before deposition, the ZnO nanorods growth follows a vapor-solid (VS) growth process [10]. Zn vapor is produced during carbothermal reduction of the ZnO powder at high temperature (1100℃). It is then oxidized soon and condenses

on the substrate to form ZnO nuclei. As the Zn vapor is continuously provided and oxidized, ZnO nanorod arrays are then assembled on top of the previously formed nucleus and grew in outward continually. All the nanorod arrays show the feature of hexagonal prisms. The uniform hexagonal prismatic growth morphology can be explained by the "lowest energy" argument, i.e., the hexagonal (0001) plane of ZnO with wurtzite structure is the closest packed plane in the crystal, and the staking along the [0001] direction therefore becomes energetically favorable [10]. This is consistent with observation that all the nanorods have crystalline [0001] growth direction.

5.3.2 Variation on the substrate surface coverage and nanorods size

The concentration of ZnO vapor in the system plays an important role in determining both the substrate surface coverage and nanorods size. As oxygen is introduced into the system, more Zn vapor is oxidized to ZnO, so that both the substrate surface coverage and nanorods size increase. With the presence of an additional small quartz tube, local concentration of ZnO vapor (within the small tube) is increased, due to the confinement effect of the quartz tube. This explains the drastic increase of the substrate surface coverage by the nanorods.

Size of the nanorods is also affected by their deposition temperature. As

temperature decreases, saturated ZnO vapor pressure in the system falls down. More ZnO vapor will transform to solid phase at lower temperature zone, leading to the production of nanorods with larger size. With the presence of the small quartz tube, this phenomenon is rather obvious, as sufficient ZnO vapor supply enhances the difference among various temperature zones.

5.3.3 Nanorod's orientation

Nucleation at the initial stage has a crucial role in alignment of the nanorods. At the initial stage, small ZnO particles nucleate on the substrate, with their (0001) plane randomly oriented, i.e. some parallel with the substrate surface while some incline with the substrate surface. Subsequently, the ZnO nanorods formed by stacking the (0001) planes have random orientations, i.e., some rods are vertically aligned while others aslant stand on the substrate (Figure 5-9a).

In the first two cases, i.e. without presence of a small quartz tube, we note on partial regions of the substrate, a ZnO flim is deposited before the nanorods growth, which can act as a buffer layer for nanorod nucleation and growth. The film contains some regions with rather flat top surface, as shown in figure 5-9b. Near hexagonal shape of the region and ZnO nanorod vertically standing on it indicate the top surface is (0001) plane. Those regions provide well stages for the ZnO

nanorods nucleation and aligned growth. Local increase on amount of vertically aligned ZnO nanorods is very likely caused by presence of such buffer layer.

With the presence of a small quartz tube, a polycrystalline ZnO buffer layer in between the ZnO nanorod arrays and substrate can be clearly observed, as demonstrated by the top view and side view SEM images in figure 5-10. At higher temperature zone, such film is rough, with (0001) planes of each grain disordered arranged, leading to the random orientations of the nanorods grown on top. When the temperature decreases, the film tend to become smoother, more grains in the film tend to be vertically aligned as well, with their (0001) faces exposed on the top surface. ZnO nanorods grown on such buffer layer are thus more aligned.

5.3.4 CL properties and crystal quality of the ZnO nanorods

For the ZnO nanorods that were prepared when the small quartz tube was employed, variation on the CL properties reveals their crystal quality's evolution with the deposition temperature. The orangish-red emission (with center ~ 620 nm) is commonly assigned to defects related to excess oxygen in ZnO [17]. At the lowest deposition temperature, a large amount of such defects exist in the structure, as indicated by the strong and broad emission peak. As the temperature increases, this kind of defects is gradually eliminated; instead, defects responsible for green

emission become dominant. For the origin of green emission, a number of hypotheses have been proposed, such as singly ionized oxygen vacancy V_o^+, V_o^{2+} center, oxygen antisite, and zinc vacancy V_{Zn} [17], which is highly controversial. Nevertheless, as the temperature further increases, the green emission is depressed and band edge emission enhances, indicating an improved crystal quality. The whole process suggests higher deposition temperature (~ 630℃) leads to a better crystal quality, as higher temperature can help to reduce the native point defect formation in the ZnO nanorods.

For nanorods synthesized in the first two cases (base pressure of 3.5 x 10^{-2}Torr, w/o oxygen presence during the nanorod array growth), their emission property indicates large amount defects still exist in the structure, although their deposition temperature is high enough (~ 630℃). This suggests sufficient ZnO vapor source supply during the nanorod growth is also important to a better crystal quality. In addition, for these nanorods (with diameter smaller than 100 nm), surface defect luminescence could also make a contribution as their surface to volume ratio is increased.

5.4 Conclusions

In summary, we have studied a catalyst free vapor phase deposition approach to

fabricate aligned ZnO nanorod arrays on Si substrate. By varying the synthesis conditions, the average diameter of the ZnO nanorods can be tuned from less than 40 nm to larger than submicron. The employment of an additional small quartz tube in the original vacuum tube furnace setting could dramatically increase the areal coverage of the substrate by nanorod arrays. Larger-diametered nanorods that grow on higher temperature zone are found to possess higher band edge to defect emission ratio.

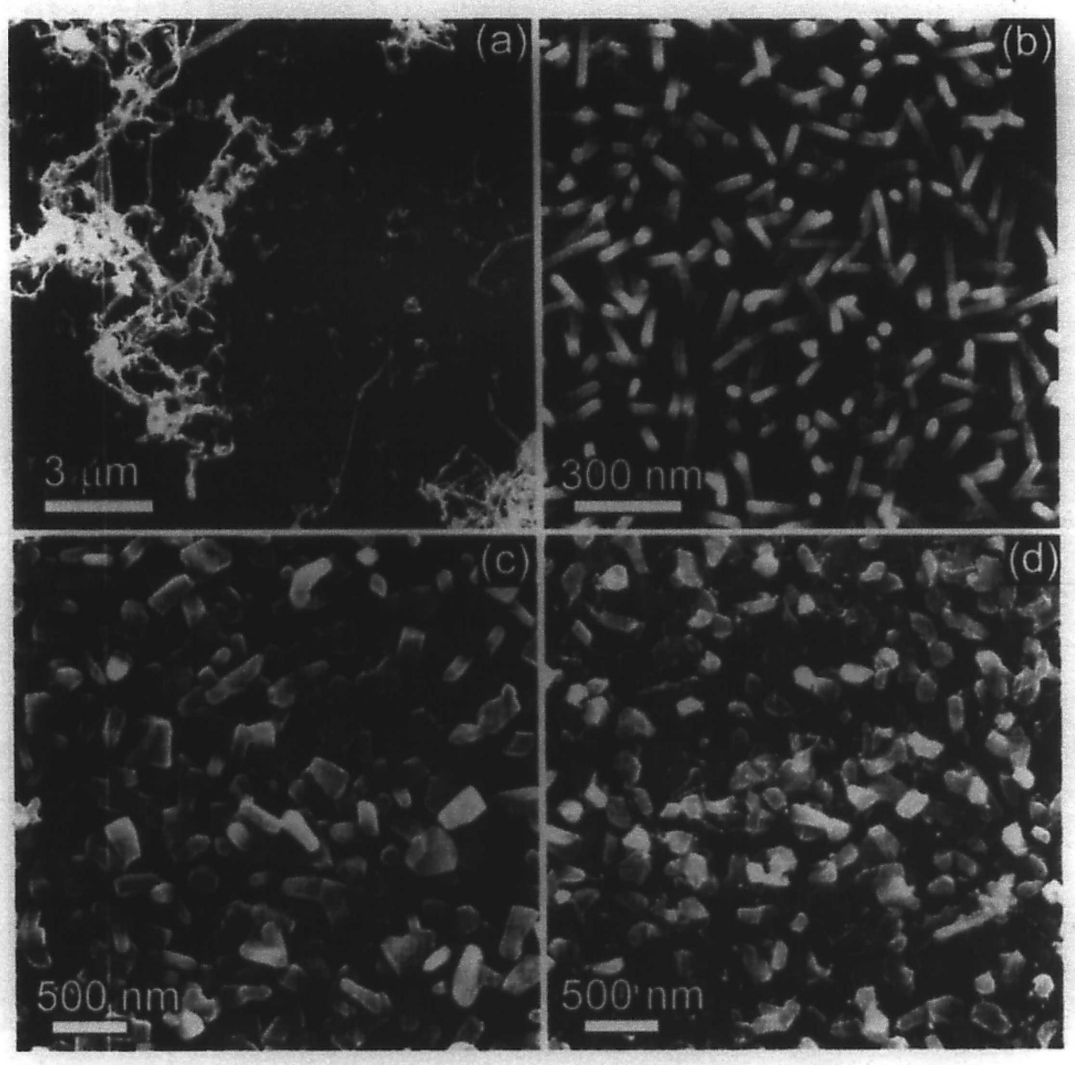

Figure 5- 2 SEM images of products fabricated at different vacuum base pressures: (a) 8×10^{-3} Torr, (b) 3.5×10^{-2} Torr, (c) 7×10^{-2} Torr, and (d) 1×10^{-1} Torr.

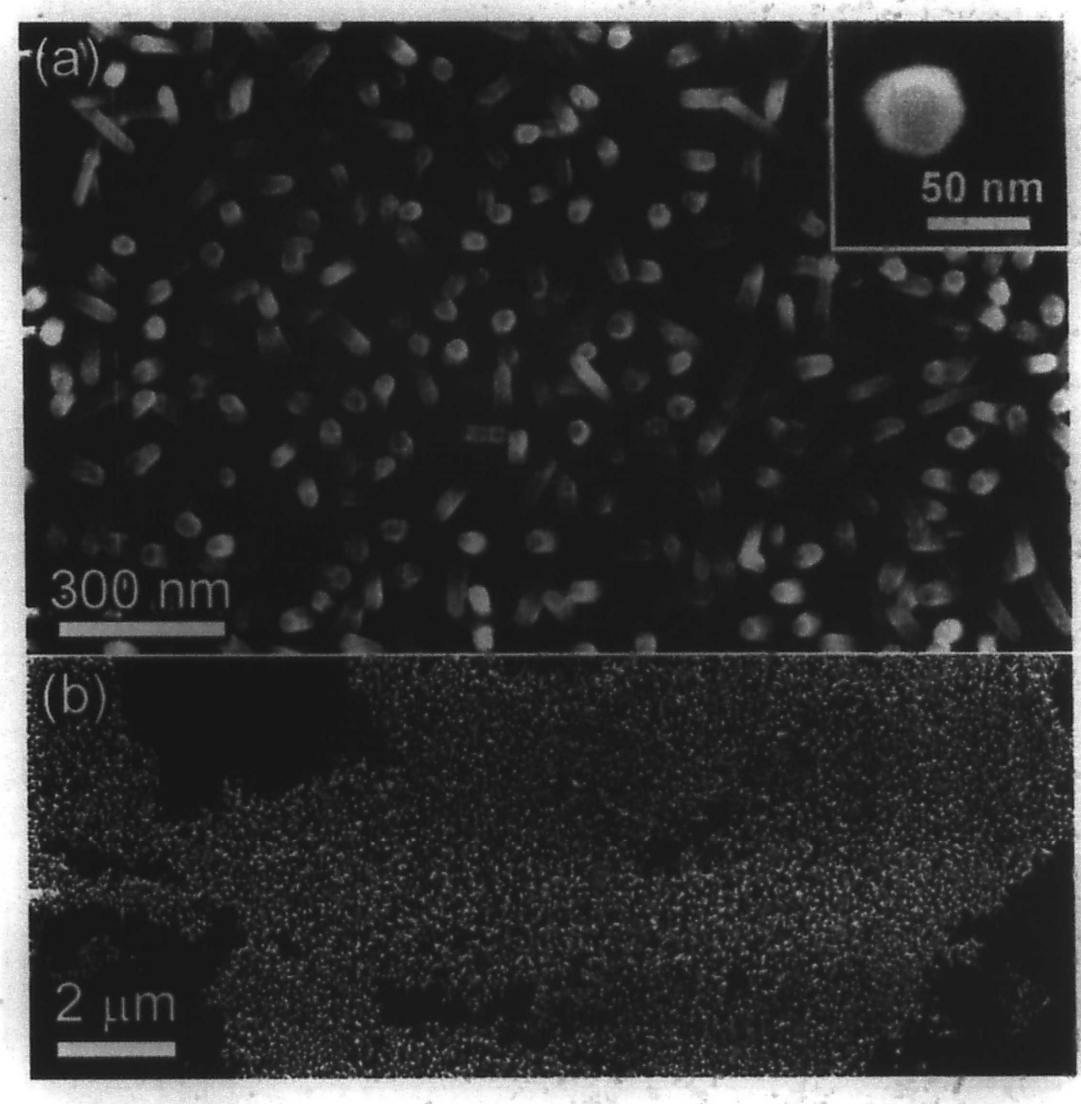

Figure 5- 3 SEM images taken from specimen synthesized when the base vacuum is maintained at 3.5×10^{-2} Torr. Its deposition temperature is around 630℃

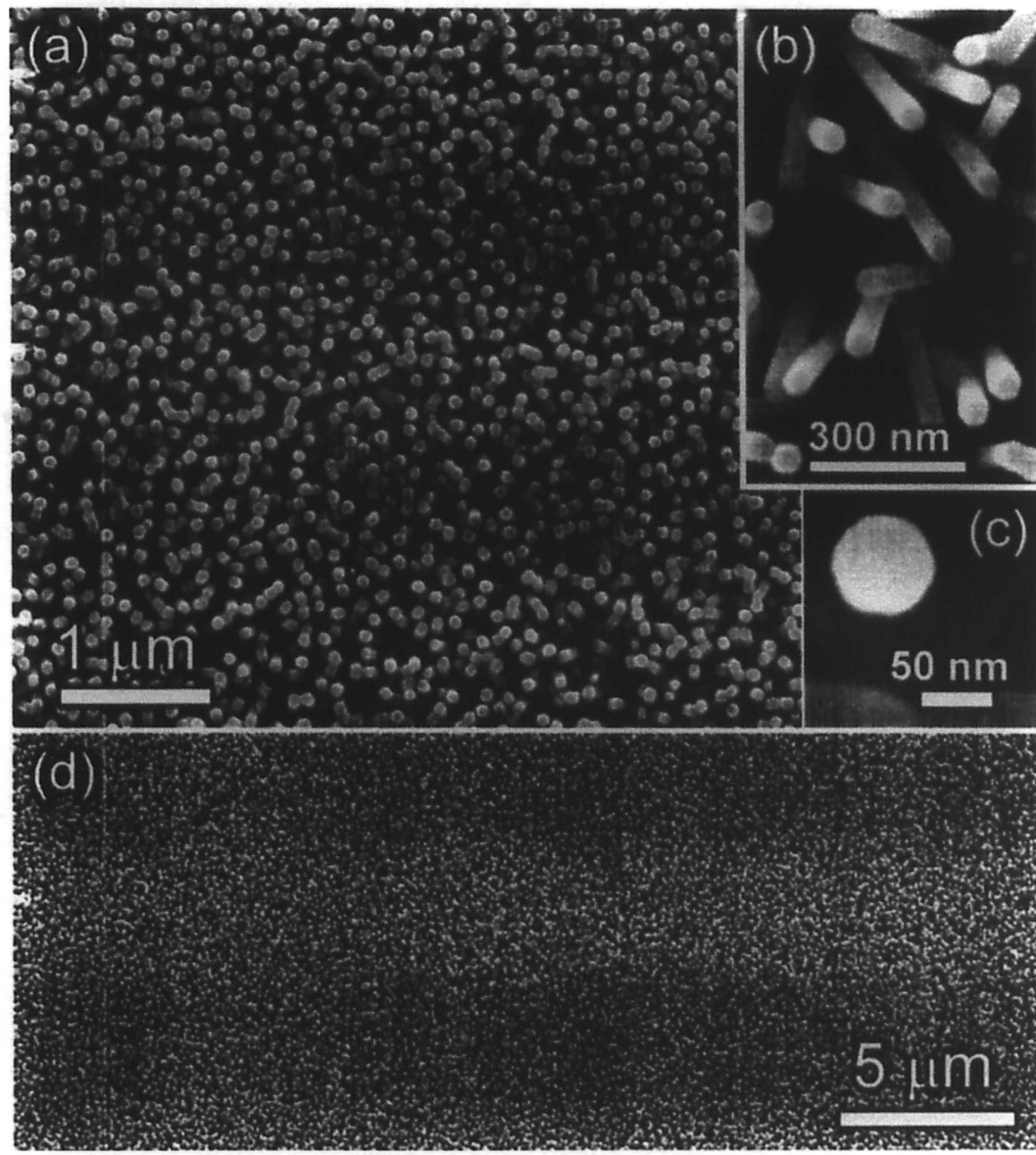

Figure 5- 4 SEM images taken from specimen synthesized with O_2 presence during the nanorod growth. The base vacuum was previously maintained at 3.5×10^{-2} Torr. Its deposition temperature is around 630℃

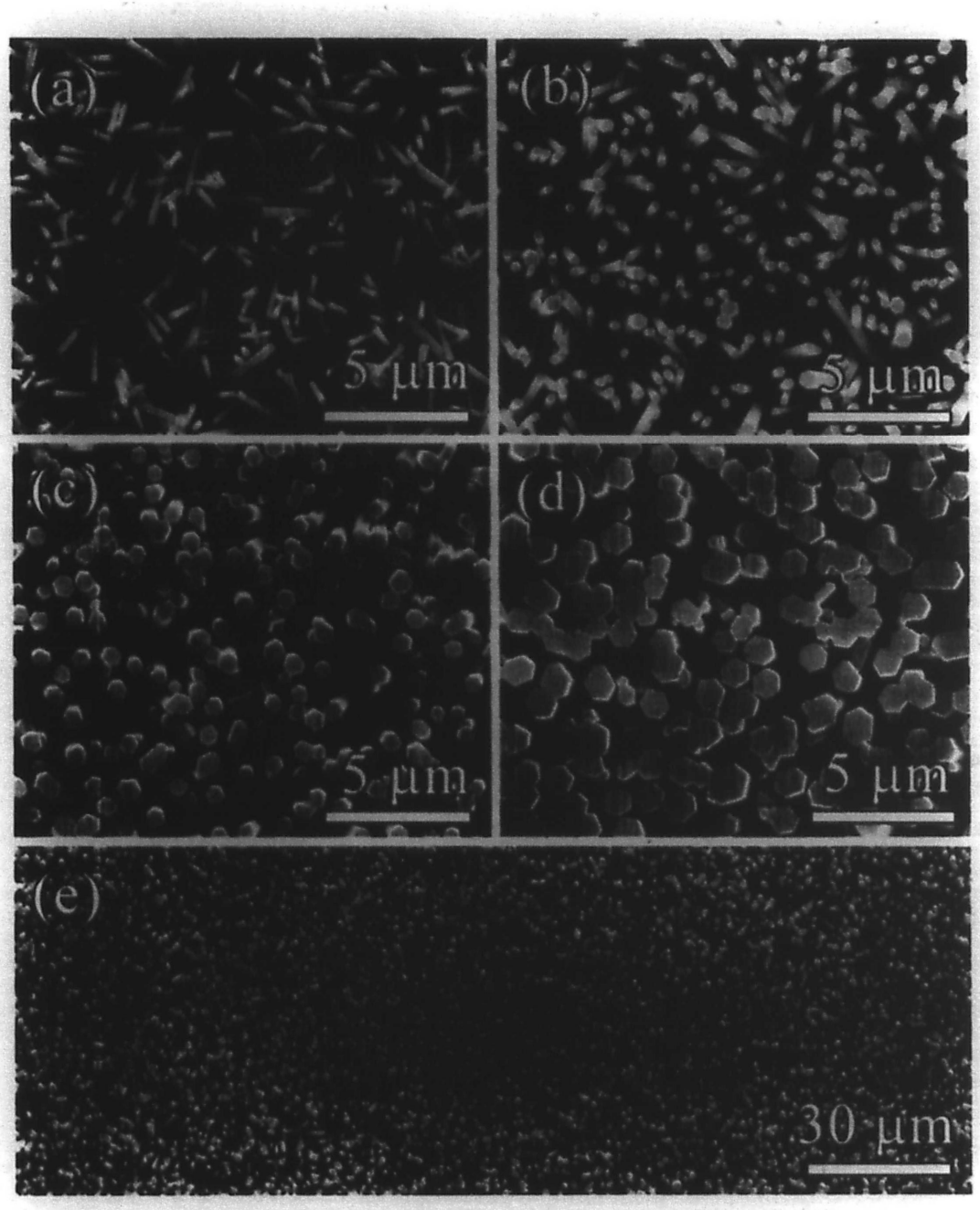

Figure 5- 5 SEM images taken from specimen synthesized with the assistance of a small quartz tube. The base vacuum was previously maintained at 3.5×10^{-2} Torr. Images (a) to (d) are taken from samples deposited at different temperature zones of (a) 630℃, (b) 616℃, (c) 606℃, and (d) 590℃, respectively. (e) is partially cut from a low magnification SEM image taken from the vertically aligned nanorod arrays, showing its large area and uniformity.

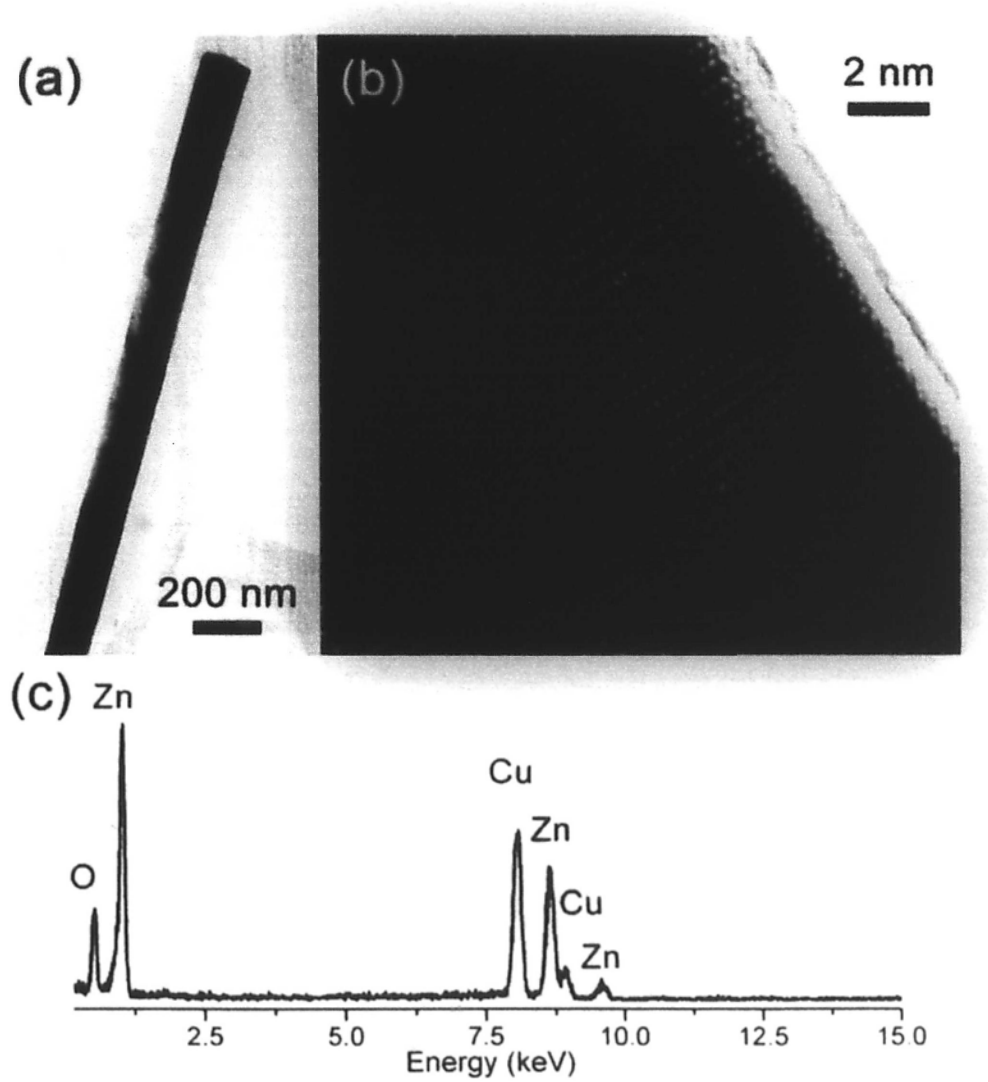

Figure 5- 6 (a) Low magnification TEM image of single nanorod. (b) High resolution TEM image taken at the surface region of single nanorod. (c) EDX spectrum taken on the nanorod.

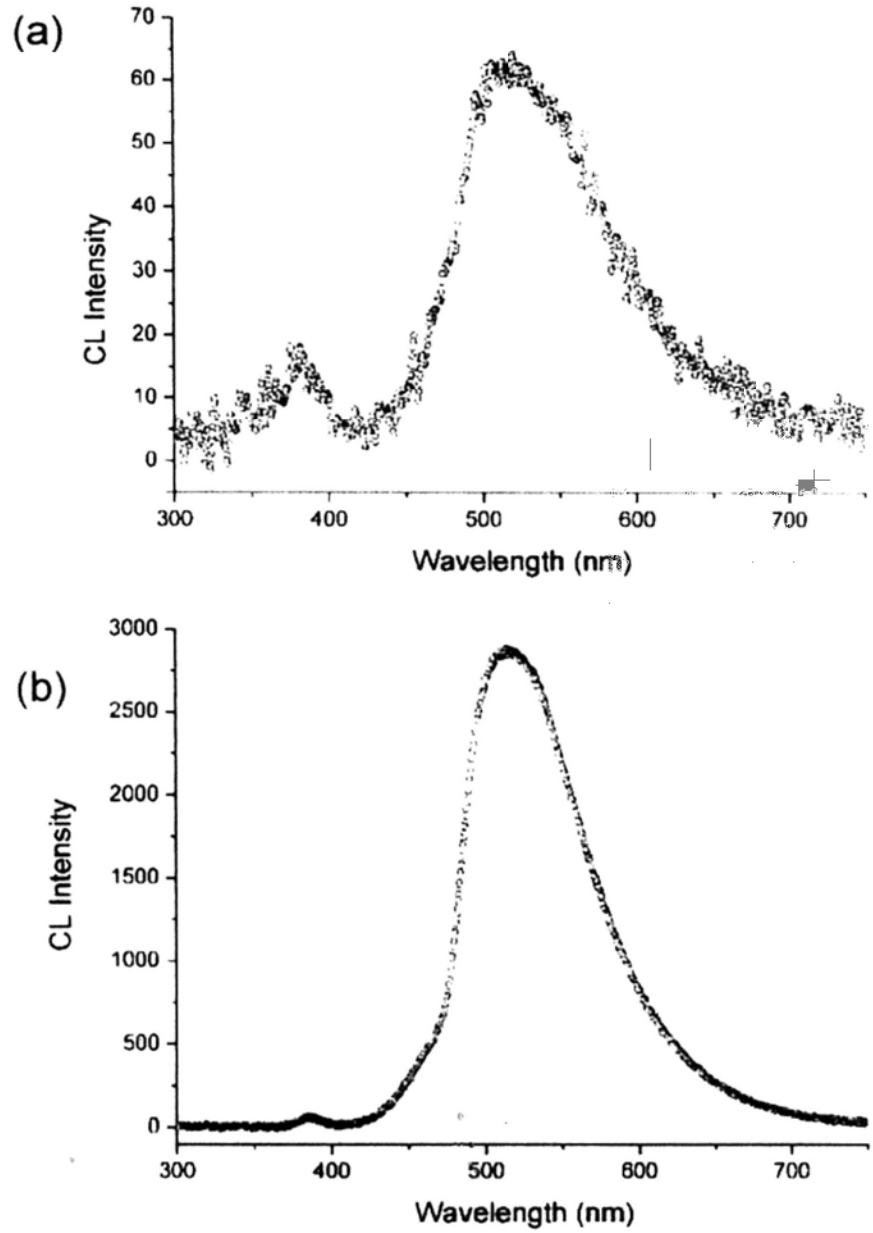

Figure 5- 7 Room temperature cathodoluminescence spectra of the ZnO nanorod arrays synthesized at (a) 3.5×10^{-2} Torr base vacuum, and (b) with additional 20 sccm O_2 flow. Deposition temperature for both specimens is ~ 630℃.

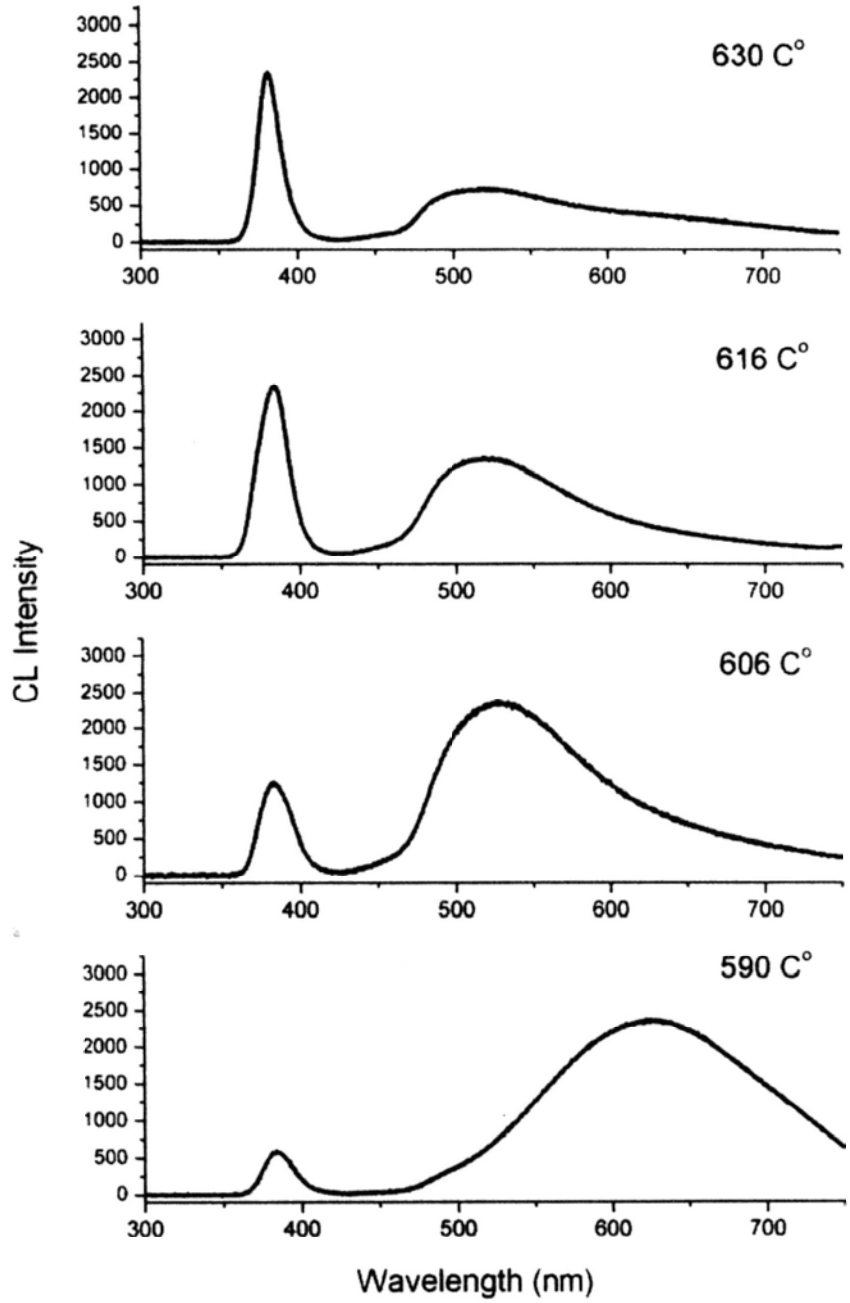

Figure 5- 8 Room temperature cathodoluminescence spectra of the ZnO nanorod arrays deposited at different temperature zones. Insets are corresponding deposition temperatures for each specimen. All the specimens are synthesized at 3.5×10^{-2} Torr base vacuum and with the presence of a small quartz tube.

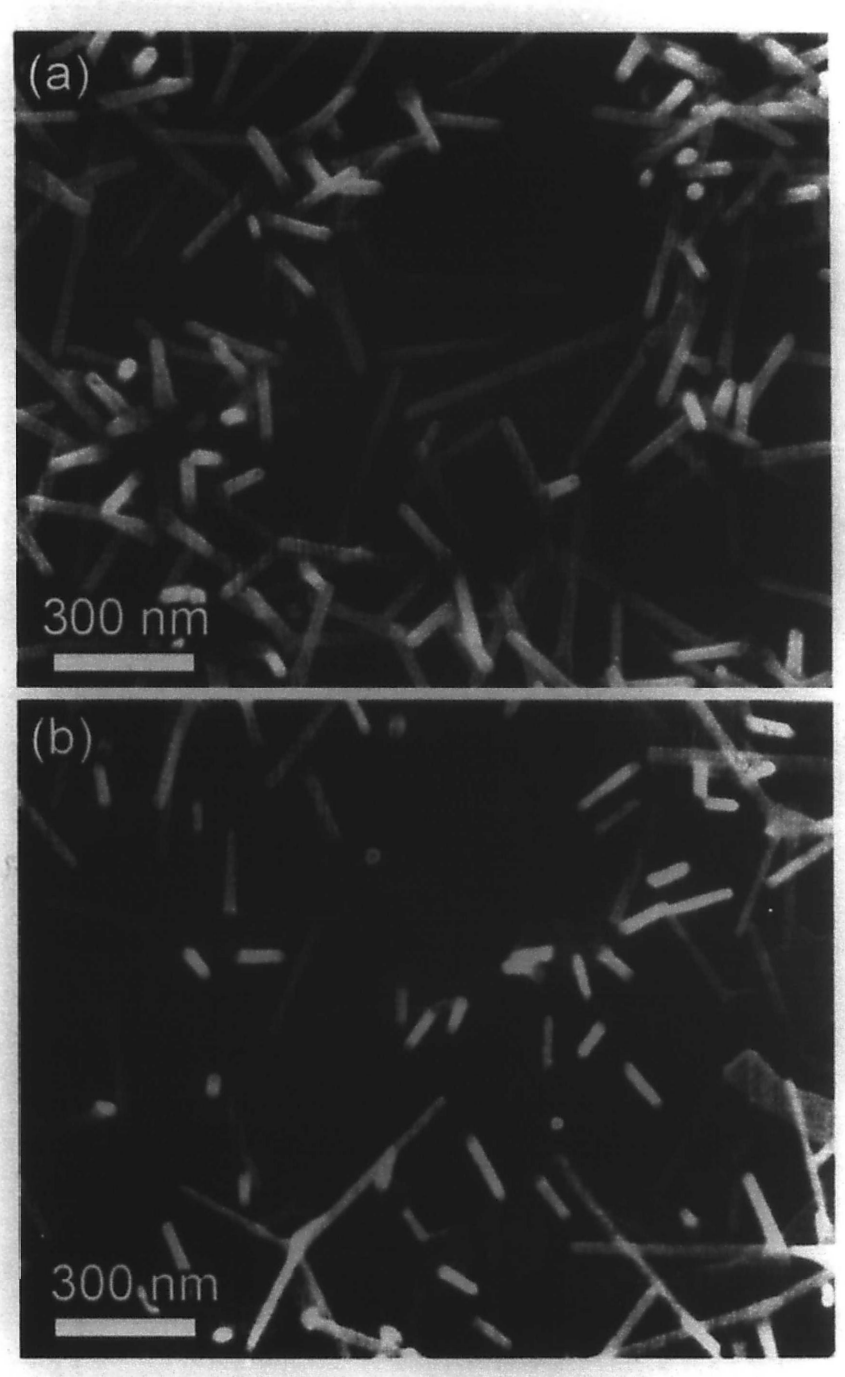

Figure 5- 9 (a) SEM image of randomly oriented ZnO nanorods. (b) SEM image showing ZnO nanorods growing from ZnO buffer layer. Both specimens are synthesized at a vacuum base of 3.5×10^{-2} Torr.

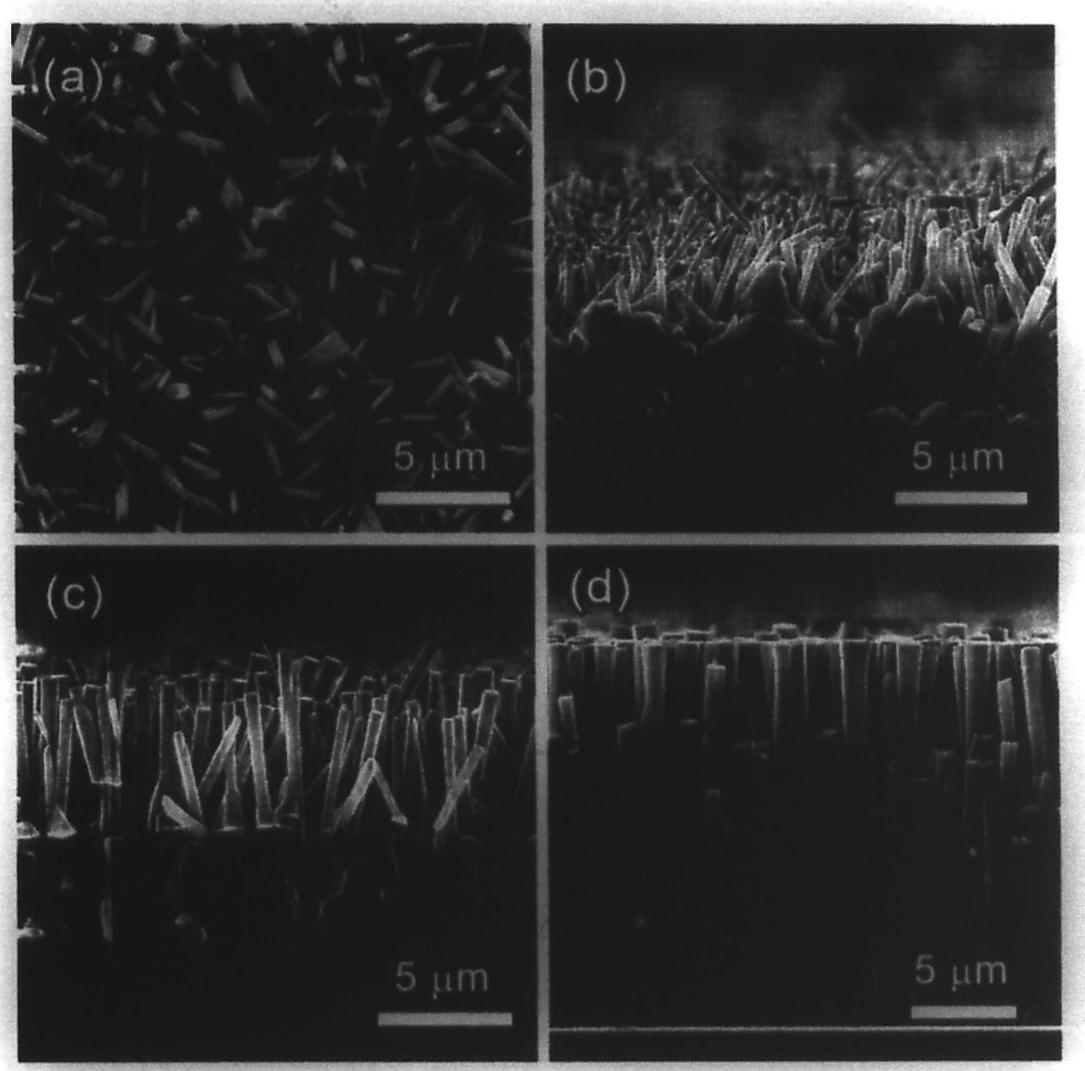

Figure 5- 10 (a) Top view SEM image of a sparse ZnO nanorod array grown on a thick ZnO buffer layer, showing the rough top surface of the buffer layer. Its deposition temperature is around 635℃. (b)-(d) Side view SEM images on ZnO nanorod arrays growing on ZnO buffer layer with deposition temperature of (b) ~ 615℃, (c) ~600℃ and (d) ~580℃, respectively. All the specimens are synthesized with presence of a small quartz tube.

Chapter 6 Suppression of Green Emission in ZnO Nanorods—a discussion on surface and interior structural quality manipulation

In last two chapters, we have noted that strong green emission can be observed from some of the ZnO nanorods prepared by both methods, i.e., the solvothermal and the thermal evaporation methods. The green emission is commonly attributed to the surface defect emission of nanostructure due to its large surface to volume ratio. In this chapter, we modify surface of the nanorods with SiO_2 and investigate the relation between green emission and the surface defect.

6.1 Experiment

ZnO nanorods which exhibit strong green emission and are prepared by the thermal evaporation method were directly used in the experiment. ZnO nanorods synthesized by the solvothermal approach were intentionally grown on a heat-resistant substrate—copper, due to the later high temperature requirement during the surface layer growth process [43]. First, a thin Zn layer was plated on a Cu foil using an acidic chloride zinc solution. Then the foil is added to a mixed aqueous solution of NaOH and H_2O_2, which is filled in a stainless steel Teflon-lined autoclave. After the autoclave was sealed, it was kept at a constant temperature in an oven for several hours until the Zn layer was exhausted. At last, the foil is taken out from the solution when the system returns to room temperature, rinsed with

distilled water and dried in air.

The SiO_2 layer was deposited on the ZnO nanorods in the high temperature vacuum tube furnace by vapor transport deposition. SiO powder was placed at center of the tube and thermal evaporated at 1000℃. The ZnO nanorods were placed at the downstream of the tube, with temperature at ~680℃-650℃ zone when the center temperature reaches 1000℃. Initially, pure Ar was used as carrier gas and the total pressure in the system was kept as 300 mbar. After 30 min evaporation and deposition, the carrier gas was switched to pure O_2 and the total pressure in the system was kept slightly larger than 1atm for 2h.

6.2 Results

Figure 6-1 (a) and (b) show the low magnification TEM images taken from the as-synthesized specimens by evaporation, and solvothermal method, respectively. The nanorods prepared by the evaporation method have an average diameter of ~150 nm while those prepared by the solvothermal method have smaller average diameter, ~ 30nm. All nanorods have the hexagonal structure, growing along the ZnO [0001] crystalline direction (Figure 6- 1c and Figure 6- 1d), and their outer surface appears to be smooth.

After depositing the SiO_2 surface layer, the morphologies of both specimens are

not destroyed. Figure 6- 2 (a) and (b) are typical high resolution TEM images taken from the surface modified nanorods. It can be seen that a ~2nm thick amorphous layer was uniformly grown on the surface of the single crystalline nanorod. EDX analysis (Figure 6- 2c), which was performed by focusing a ~2nm electron beam probe on the amorphous layer, reveals the thin layer contains Si and O only. Electron energy loss spectra were taken by focusing the electron beam on the amorphous surface layer and the core of the same nanorod, respectively. In Figure 6- 2d, signature of the Si L edge fine structure as in SiO_2 (Si^{4+}) [44,45] is observed, with an onset at 106 eV and a later peak centered at 108 eV, suggesting the amorphous surface layer is composed of SiO_2. When the electron probe is moved to the core region of the specimen, energy loss signals from the O K edge and the Zn L edge can also be observed (Figure 6- 2e), which is consistent with the existence of the ZnO nanorod core [46]. Over the hundreds of nanorods examined, the surfaces of all of them have been uniformly covered with a thin layer of SiO_2.

Typical room temperature cathodoluminescence spectra of nanorods prepared by different methods are shown in Figure 6- 3 and Figure 6- 4, respectively. Besides the band edge emission at ~385 nm, the as synthesized nanorods by evaporation show a broad green emission with an intensity maximum at ~530 nm (Figure 6- 3a). When the surface of these nanorods was deposited by a thin layer of SiO_2, the green

emission was only slightly depressed without any obvious change on the peak line shape (Figure 6- 3b). The major peak features in the spectra of the solvothermal ZnO nanorods and their evolution after the surface modification are rather similar to those by evaporation methods, i.e., a band edge emission at ~ 385 nm and a green emission, and the green emission is slightly weakened when the surface of the solvothermal ZnO is covered with SiO_2. Nevertheless, one shall notice that a much smaller band edge to green emission ratio exists in the solvothermal nanorods, as compared to that of the evaporation ones. In addition, the green emission bands are broader in the solvothermal nanorods, with a peak maximum shifting to 570 nm (Figure 6- 4a). When the nanorod surface is deposited with a thin layer of SiO_2, obvious narrowing of the defect emission in the visible range is observed, with its peak center blue shifted to ~530 nm, which is the same as the evaporated ZnO nanorods (Figure 6- 4b).

6.3 Discussion

We first discuss the possible origin of the green emission in the ZnO nanorods. In the literature, Cu impurity in ZnO has been reported to induce a green luminescence [47-49]. However, Cu signal was not found in our specimen, when analyzed using secondary ions mass spectroscopy (SIMS). With the measurement

sensitivity in the range of several ppm and below, such result suggests the absence of the Cu impurity in our sample. In addition, the emission originated from the interstitial Cu has a maximum at ~510 nm, being different from that observed in our samples. The other common explanation for the green emission is the intrinsic defects involving O and Zn [50,51], which is likely the explanation for the green emission in our specimen. For nanorods synthesized by solvothermal method, the much broader peak in the visible range indicates contribution from not only the green emission, but also yellow and orange luminescence as well. The yellow and orange emissions were commonly assigned to defect related to the presence of -OH groups, which is easily introduced, in particular, at the surface of the nanorods, during the solvothermal process.

When the surface of the as-synthesized nanorods are deposited with a thin layer of SiO_2, the reduction on green emission indeed suggests that surface passivation would suppress the defect emission and thus increase the band edge to defect emission ratio. This is usually explained as termination of dangling bonds on the ZnO nanorod surface [52] by the surface SiO_2 layer. Nevertheless, one shall notice that such surface modification fails to significantly reduce the green emission centered at ~530 nm, which results suggested that the deep level defects contributing to the green emission may not only be limited on the nanorod surface, but also in the

interior of the ZnO nanorods.

We have prepared control specimens by treating the as-prepared ZnO nanorods at the same condition of SiO_2 surface layer growth, but without introducing the SiO source. In fact, such a treatment is similar to annealing the as-prepared samples at 650°C in an oxygen atmosphere. Such annealing process indeed modifies the luminescence behavior of the nanorods (Figure 6- 5 & Figure 6- 6). We have found that the green emission from the control sample is enhanced for both types of ZnO nanorods after the annealing. In addition, narrowing and blue-shifting (peak center from ~570 nm to ~530 nm) of the defect emission is observed in the annealed solvothermal ZnO nanorods sample.

The results suggest that the annealing process could remove the –OH type of defects in the solvothermal ZnO sample, which is reasonable. On the other hand, the annealing process fails to repair the O-related defects in the samples. In fact, whether these defects can be repaired would depend on both the O partial pressure and the temperature during annealing. Consequently, one can see that the introduction of the SiO_2 surface layer indeed suppress the O-related defect emission to some extent, but not significantly. This further indicates that these defects not only locate on the surface of the nanorods (which should be largely passivated when the surface SiO_2 is introduced), but also in the interior of the nanorods.

6.4 Conclusions

Passivating the ZnO nanorod surface with a thin SiO_2 layer fails to significantly depress the green emission in both types of ZnO samples. This suggests that surface defects, although contribute to, but may not be mainly responsible for the intense green emission observed in the ZnO nanorods. The interior structure quality, which is sensitive to the preparation method and conditions, plays important roles in determining the luminescence behavior of the ZnO nanostructures.

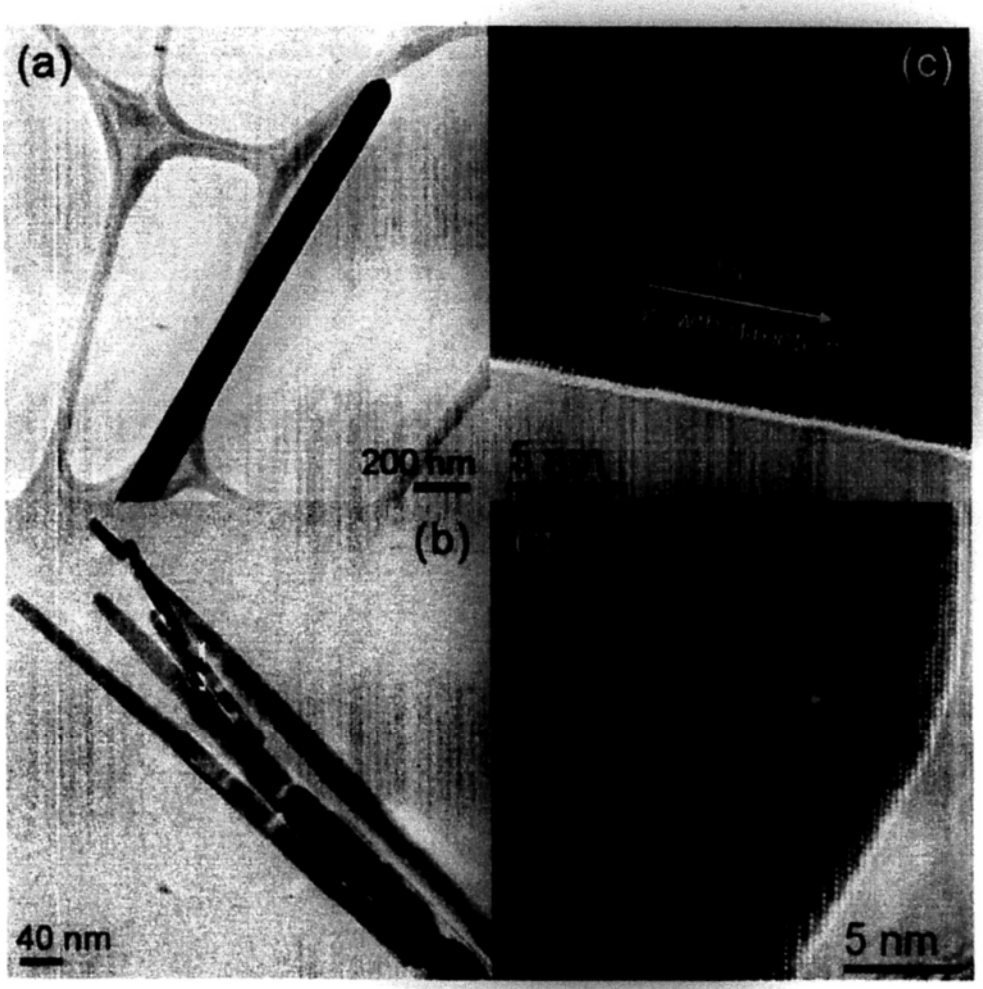

Figure 6- 1 (a), (b) Low magnification TEM images showing the general morphology of the as synthesized ZnO nanorods by thermal evaporation, and solvothermal method, respectively; (c), (d) High resolution TEM images take from ZnO nanorods shown in (a), and (b), respectively.

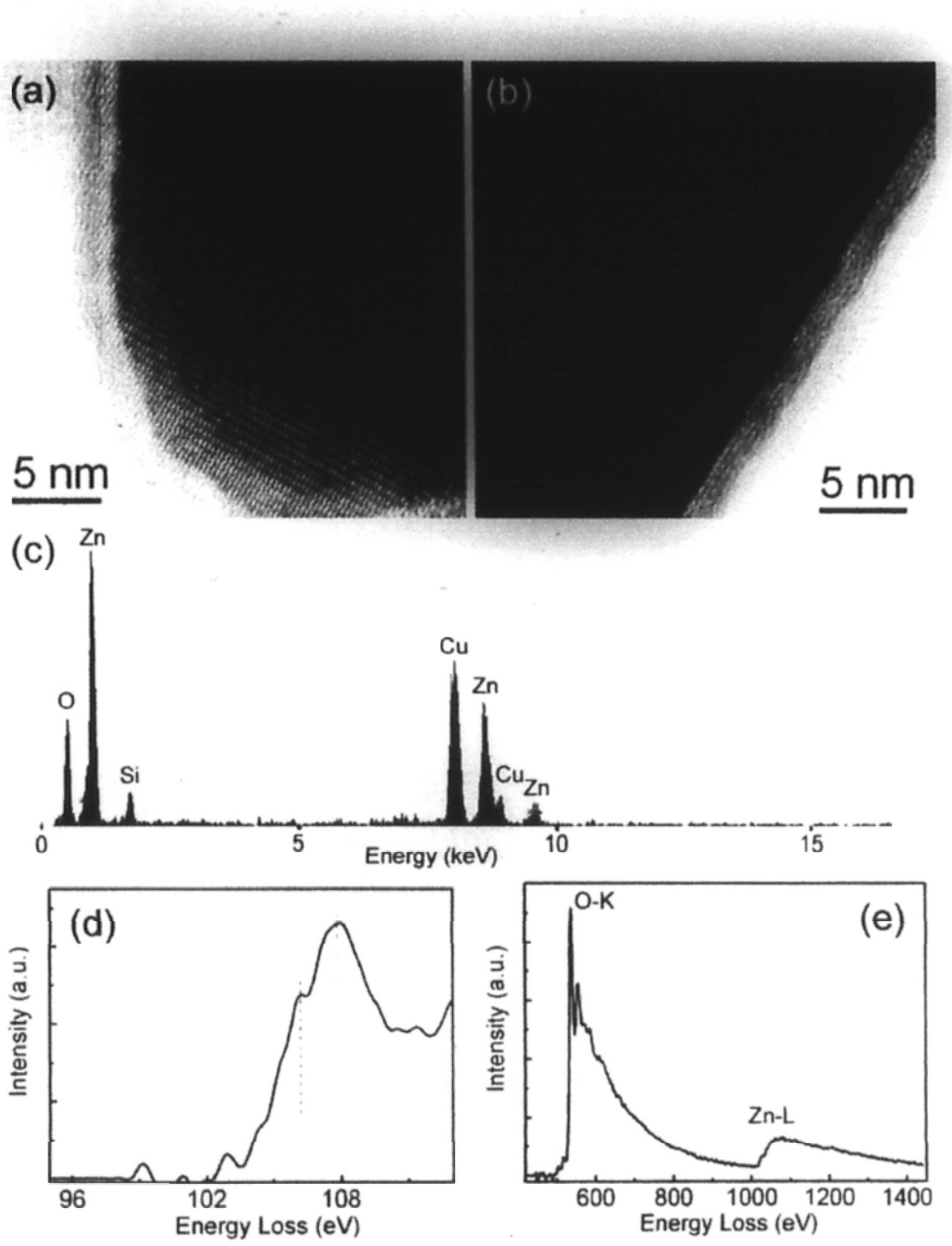

Figure 6- 2 (a) and (b) High resolution TEM images taken on the ZnO nanorod with a SiO_2 surface layer; (c) EDX spectra taken by focusing the electron beam on surface region of the sample; (d) EELS taken by locating the electron beam at the surface layer of the ZnO nanorod; (e) EELS taken by locating the electron beam at interior of the ZnO nanorod. The O-K edge and Zn-L edge can be clearly observed.

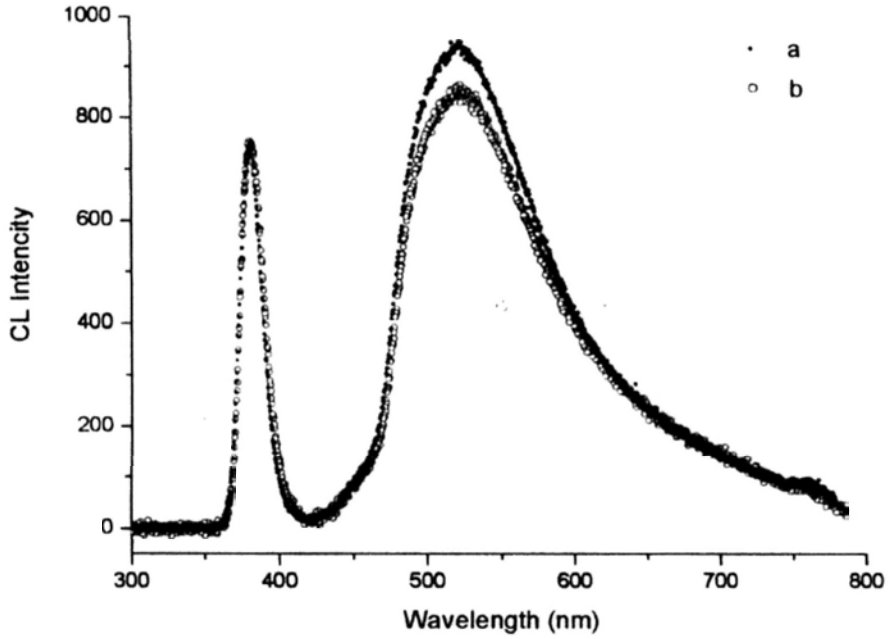

Figure 6- 3 Room temperature CL spectra taken from (a) as-synthesized ZnO nanorods, (b) ZnO nanorods with SiO_2 surface layer. The nanorods were synthesized by thermal evaporation method. The spectra were normalized using the band edge emission.

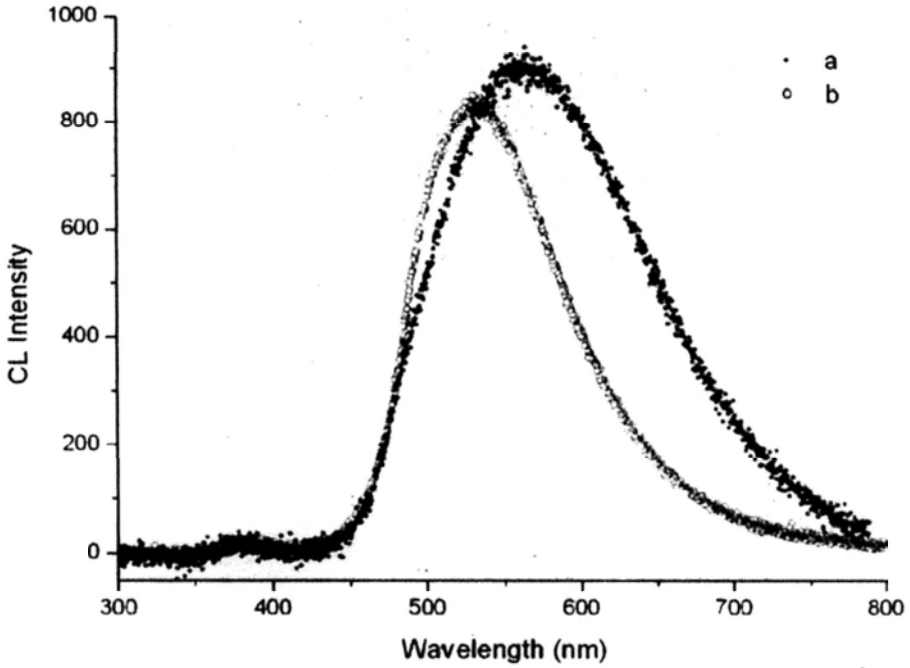

Figure 6- 4 Room temperature CL spectra taken from (a) as-synthesized ZnO nanorods, (b) ZnO nanorods with SiO_2 surface layer. The nanorods were synthesized by solvothermal method. The spectra were normalized using the band edge emission.

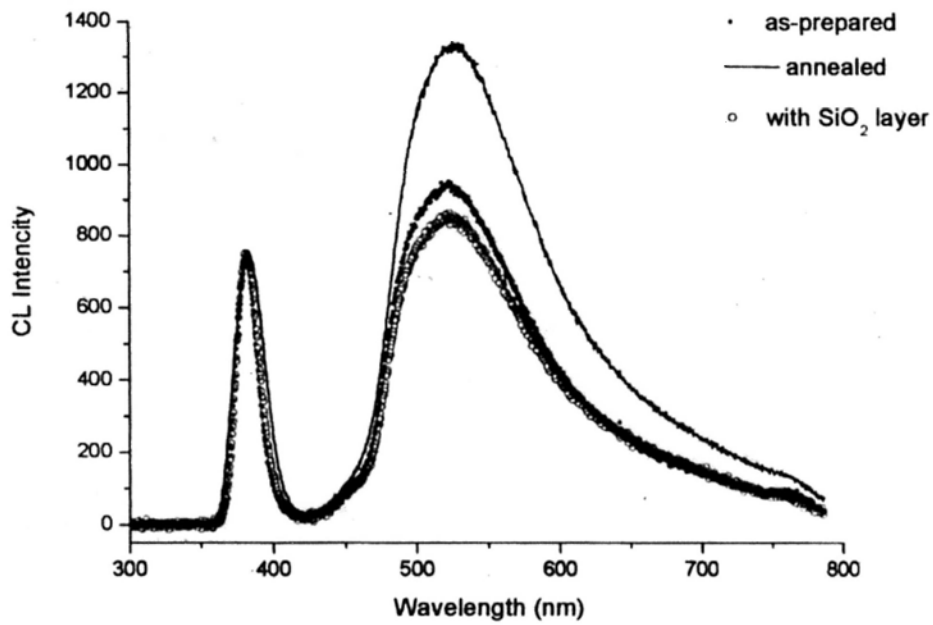

Figure 6- 5 Comparing the room temperature CL property of the control sample (marked as annealed) with that of the as-prepared ZnO nanorods and ZnO nanorods with SiO_2 surface layer (The nanorods were synthesized by thermal evaporation method. The spectra were normalized using the band edge emission.)

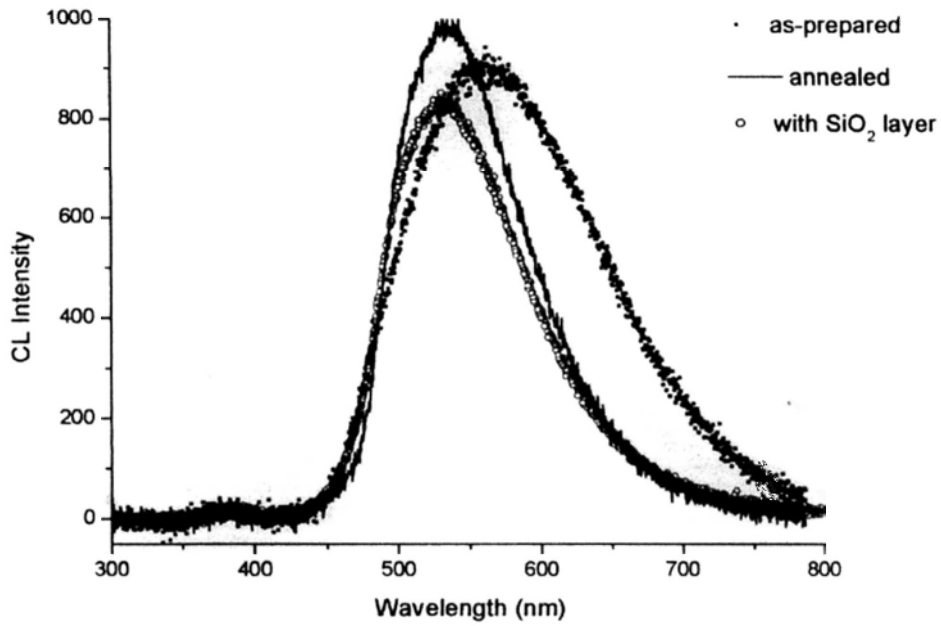

Figure 6- 6 Comparing the room temperature CL property of the control sample (marked as annealed) with that of the as-prepared ZnO nanorods and ZnO nanorods with SiO_2 surface layer (The nanorods were synthesized by solvothermal method. The spectra were normalized using the band edge emission.)

Chapter 7 ZnO / $Cd_xZn_{1-x}S_ySe_{1-y}$ Core-shell Nanocable Arrays on ITO for Photovoltaic Devices

In this chapter, we developed a thermal evaporation method that modifies the surface of ZnO nanorods and forms core shell structure. SEM and TEM characterization on the specimen reveal that the surface of single crystalline ZnO nanorod in an array configuration is uniformly covered by polycrystalline II-VI compound alloy surface layer. XRD analysis reveals the wurtzite structure for both the core and shell materials. The band gap of the shell can be systematically tuned from 2.5 to 1.7 eV by varying its composition, as suggested by the optical extinction measured of the samples. The type II band alignment between the ZnO core and the alloy shell enables effective photo-generated charge carrier separation, and the single crystalline ZnO nanowire array provides a direct electrical pathway for the photo-injected electron transport. The nanocable solar cells exhibited short-circuit current ~0.2 mA/cm^2 and open-circuit voltages of 0.45 V when illuminated with 100 mW/cm^2 simulated AM 1.5 spectrum.

7.1 Experiment

The ZnO nanorod arrays on ITO substrate were synthesized using the similar strategy described in Chapter 5, by carbon thermal reduction of ZnO in the high

temperature vacuum tube furnace. Briefly, mixed powders of ZnO and C were placed at center of the alumina tube in the furnace; ITO substrates were placed in the downstream of the tube. Then the tube was sealed and pumped up to 4×10^{-2} Torr. 100sccm pure Ar was introduced into the system as the carrier gas. Total pressure in the system was kept at 300 mbar for the whole process. The furnace was then heated up to 1100℃ and kept at the same temperature for 1h. The sample was taken out from the furnace after the furnace was cooled down to room temperature [53].

The CdSSe layer was deposited on the ZnO nanorod surface in the same high temperature vacuum tube furnace by vapor transport deposition. Mixture of CdSe and CdS powder with different molar ratios was placed at center of the tube and thermal evaporated at 850℃. The ZnO nanorod-on-ITO was placed in the downstream of the tube, which temperature is roughly in the range of 550℃~500℃. The system was pre-pumped up to 1×10^{-2} Torr, before Ar was introduced as the carrier gas and the total pressure in the system was maintained as 300 mbar. After the being dwelled for ~30 min, the furnace was cooled down to room temperature.

In assembling the prototype solar cell device using the nanocable array-on-ITO, we used Pt-coated ITO glass as the counter electrode, which is fabricated by thermal decomposition of 5mM Chloroplatinic acid hydride (99.9+%, IL) at ~400 °C for 20

min. The cell is filled with a liquid electrolyte containing 1.8 M Na_2S and 3 M S aqueous solution, and packaged using a 60 μm thick hot melt sealing foil (SX1170-60, Solaronix). The active area of the cell was 0.30 cm^2. I-V characteristic of assembled prototype solar cell is measured when illuminated with 100 mW/cm^2 simulated AM 1.5 spectrum.

7.2 Results

Figure 7- 1a reveals the general morphology of the as-prepared ZnO nanorod arrays on ITO substrate. Nanorods with average diameter of 150 nm uniformly stand on the substrate surface. The surfaces of the nanorods appear smooth. With the shell material deposited on surface of the nanorods in the array, one can see that the nanorod surface becomes rough and its diameter obviously increases (Figure 7- 1b). Figure 7- 1c is a photograph taken from a series of ZnO/ II-VI compound alloy nanocable array specimens, which were prepared when pure CdSe powder, mixture of CdSe and CdS powder with mass ratio of 3:1 and 1:3, and pure CdS powder were used as the evaporation source, respectively. The corresponding EDX spectra taken from the four specimens are shown in Figure 7- 1d. Both O and Zn signals present in all four samples, as originating from the cores of the nanocables. While Cd always appear in the EDX spectra of the samples, a systematic ratio variation between S and

Se can be found when the specimen composition changes.

The XRD spectra of the four specimens are shown in Figure 7- 2. Diffraction peaks from the crystalline ZnO core, the shell material, and the ITO on substrate can be observed. Both the ZnO nanorod core and the II-VI shell have the wurtzite structures. In specimen #1, which was prepared using pure CdSe powder as the evaporation source, the diffraction peaks (other than those from ZnO and ITO) can be indexed to the wurtzite CdSe. When increasing amount of CdS is added to the evaporation source for sample #2, #3 and #4, shifting of the corresponding diffraction peaks is observed, suggesting the gradual increase of the lattice parameters of the II-VI compound alloys in the nanocable shell as the S content increases. One shall note that the measured lattice parameter is slightly larger than that of standard wurtzite CdS crystal, although such a sample is prepared using pure CdS powder as the evaporation source, suggesting that the composition of the shell layer may be different from pure CdS.

TEM analysis provides more detailed information on microstructure and composition of the core-shell nanocable specimens, due to the high spatial resolution associated with such a technique. All of the specimens have similar low magnification images, as shown in Figure 7- 3a. The ZnO nanorod is uniformly covered by a surface layer of ~20 nm thick. Diffraction contrast observed in the

shell layer suggests the polycrystalline nature of the shell. This is further confirmed by the high resolution TEM image (Figure 7- 3b and 7- 3c) taken from the sample. The grain size of the shell is usually in the range of several to several tens nanometers. A ~ 2 nm electron probe was used to carry out the EDX analysis in the core, and shell regions, respectively. When the electron probe was positioned at core region of the samples, all of the possible compositional elements, Zn, O, Cd, Se (S) are observed. Compositions of the shell can be found in Table 7- 1 for the four specimens, where one can see the presence of a small amount of Zn in the shell layer for specimen #2, #3, and #4, although only CdSe and/or CdS are used as the source material for the nanocable shell growth. This explains the XRD data taken from specimen #4, i.e., the lattice parameter of the shell is slightly larger than that of pure CdS due to the formation of CdZnS alloy. Together with the TEM imaging, the EDX results suggest that the specimens are ZnO-core/ $Cd_xZn_{1-x}S_ySe_{1-y}$ -shell nanocables.

Table 7- 1 Experimental shell composition and band gap for the four specimens

Sample No.	#1	#2	#3	#4
Composition	CdSe	$Cd_{0.9}Zn_{0.1}S_{0.33}Se_{0.67}$	$Cd_{0.76}Zn_{0.24}S_{0.77}Se_{0.23}$	$Cd_{0.76}Zn_{0.24}S$
Band gap	1.69 eV	1.90 eV	2.26 eV	2.47 eV

Figure 7- 4 plots the transmittance spectra of bare ZnO nanorod arrays and the four nanocable specimens. Strong excitonic absorption induces the transmittance abruptly decreases starting at the band edge for each of the sample. One can clearly see that the spectrum from pure ZnO nanorod arrays drops around 3.3 eV, matching the band gap of ZnO. While for the nanocable specimens, the spectra fall before 3.3 eV, starting from the band edges of the corresponding shell material. For a direct band gap semiconductor, the band gap E_g obeys equation $(\alpha h\nu)^2 \propto (h\nu - E_g)$, where α is the optical absorption coefficient, and $h\nu$ is the photon energy. By plotting $(\alpha h\nu)^2$ versus $h\nu$, and extrapolating the straight portion of the plot to the energy axis at α =0, we estimated the band gap values for all compound alloy shells in the nanocable specimens (Figure 7- 5), which are also listed in Table 7- 1. As the composition changes, the band gap of the alloy shell varies from 2.5 eV to 1.7 eV.

Figure 7- 6 shows the J-V characteristics of one of the ZnO/CdSe nanocable solar cell and a cell assembled with bare ZnO nanorod arrays (inset in Figure 7- 6), which were recorded during illumination with 100 mW/cm^2 simulated AM1.5 spectrum. The ZnO nanorods assembled in the two cells are both ~ 5 μm in length. The open-circuit voltage (0.45 V) and the short-circuit current (~0.2 mA/cm^2) obtained from the nanocable solar cell are one, and two magnitude higher than those

of the bare ZnO nanorod solar cell, respectively. The power conversion efficiency improves from 0.0002% in the bare ZnO nanorod solar cell to 0.2% in the nanocable solar cell.

7.3 Discussion

7.3.1 Formation mechanism of nanocable array with tunable shell composition

Both CdS and CdSe can be vaporized at around 850℃ in vacuum (~300 mbar) and recrystallize at ~500℃ as supersaturation is achieved. If the ZnO nanorod arrays (serving as the substrate) are located at the ~500℃ temperature zone of the tube furnace, the evaporated CdS and/or CdSe can deposit on surface of the ZnO nanorods upon supersaturation. As the CdS_xSe_{1-x} alloy is stable with any x value, the simultaneous evaporation of CdS and CdSe enable us to tune the alloy composition by simply changing the mass ratio of CdS to CdSe in the evaporation source powder. With knowing the "evaporation temperature" and "crystallization temperature" of desired materials, we can use this method to form many kinds of core-shell nanocable structures. If the shell consists of complex alloy, similar "crystallization temperature" for each component is crucial.

The presence of Zn in sample #2, #3, and #4 seems strange, as Zn was not introduced as a source material during the nanocable shell growth. On the other

hand, one shall note that the Zn signal is only detected when S is introduced as the source material for shell growth. In fact, reaction between S and ZnO is possible [54], especially at elevated temperatures. During the evaporation process, decomposition of the CdS source would result in S generation, which will then be transferred to the downstream of the tube system and react with the preloaded ZnO nanorod arrays. Such a reaction would preferably occur at the surface of the ZnO nanorod, and produce to ZnS. At the same time, deposition of the Cd and Se (S) on the ZnO nanorod surface takes place, and multi-component alloys (Cd-Zn-S (Se)) are resulted. We also find that the amount of Zn increases together with the S amount increases in the source material, further supporting the argument that the Zn incorporation in the shell layer is due to the existence of S in the system.

7.3.2 Tunable absorption range and enhanced photoresponse

Band gap of the alloy shell layer can be adjusted by systematically changing their composition. This provides us a convenient way to tune the light absorption range of the nanocable structure for solar harvesting. Compared to that of the bare ZnO nanorod solar cell, energy conversion efficiency of the nanocable solar cell improves nearly one thousand times. It benefits from two reasons. One is the increased light absorption induced by presence of the shell layer. The other is the

type II alignment formed between the ZnO core and the alloy shell. That means both the conduction band minimum and the valence band maximum of the core lies below those of the shell material. Such a configuration drives the the photo-generated electrons to the ZnO side, reducing the recombination rate of electrons and holes within the photo absorbing material (i.e., the compound alloy shell).

7.4 Conclusions

Through a simple two step thermal evaporation method, we successfully fabricated a serials of core-shell ZnO / $Cd_xZn_{1-x}S_ySe_{1-y}$ nanorod arrays on ITO/glass. In the structure, single crystal ZnO nanorods are uniformly covered by polycrystalline $Cd_xZn_{1-x}S_ySe_{1-y}$ layer. Both the core and shell materials have wurtzite structures, and exhibit strong absorption on light with photon energies larger than their corresponding band gaps. Band gap of the alloy shell varies with its composition changing, which provides a convenient way to tune the light absorption range in the nanocable structure. The type II band alignment between the ZnO core and the alloy shell enables effective photo-generated charge carrier separation and the single crystalline ZnO nanorod provides a direct electrical pathway for the photo-injected electrons. The nanocable solar cells exhibited

short-circuit current ~0.2 mA/cm^2 and open-circuit voltages of 0.45 V when illuminated with 100 mW/cm^2 simulated AM 1.5 spectrum.

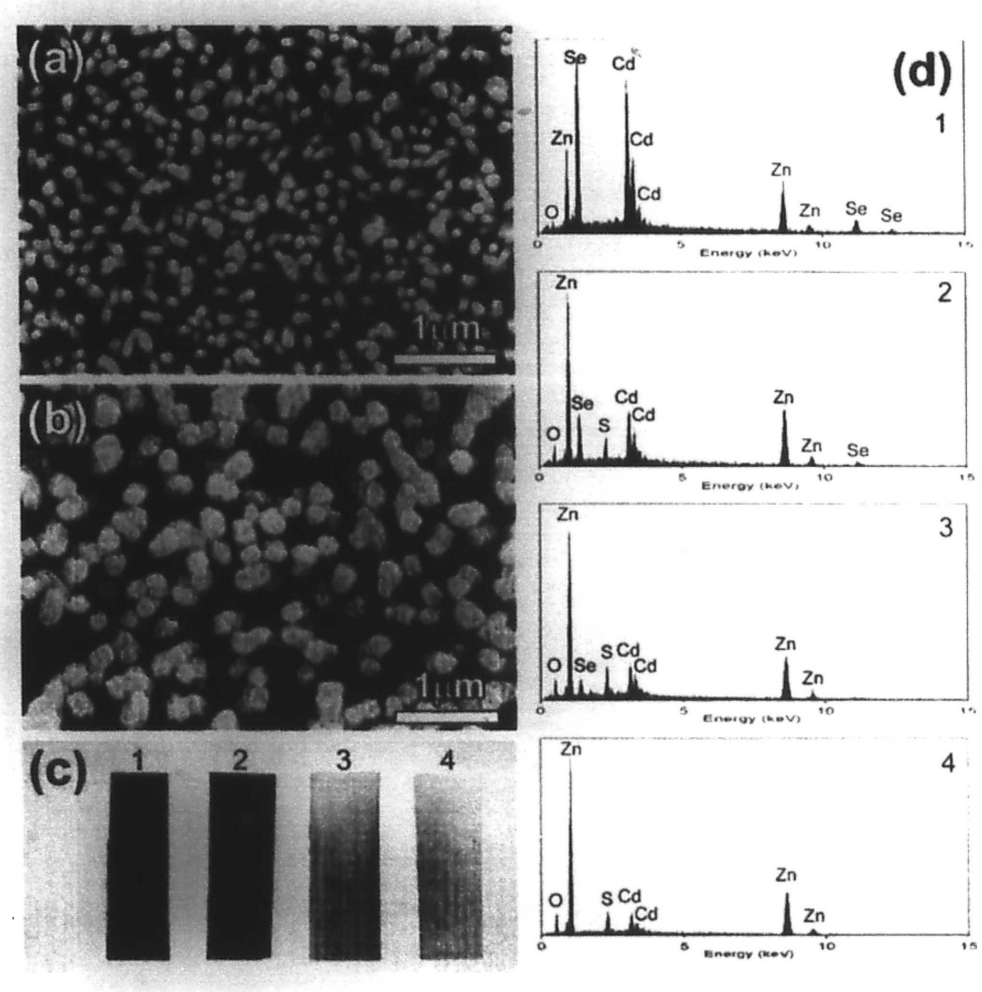

Figure 7- 1 Top view SEM images taken from (a) as synthesized ZnO nanorod arrays on ITO/glass, (b) the ZnO nanorod arrays with surface deposition of the desired material. (c) Photograph taken from a series of ZnO/ II-VI alloy nanocable array specimens, which were prepared when pure CdSe power, mixture of CdSe and CdS powder with mass ratio of 3:1 and 1:3, and pure CdS power were used as the evaporation source, respectively. (d) EDX spectra taken from the four specimens illustrated in (c).

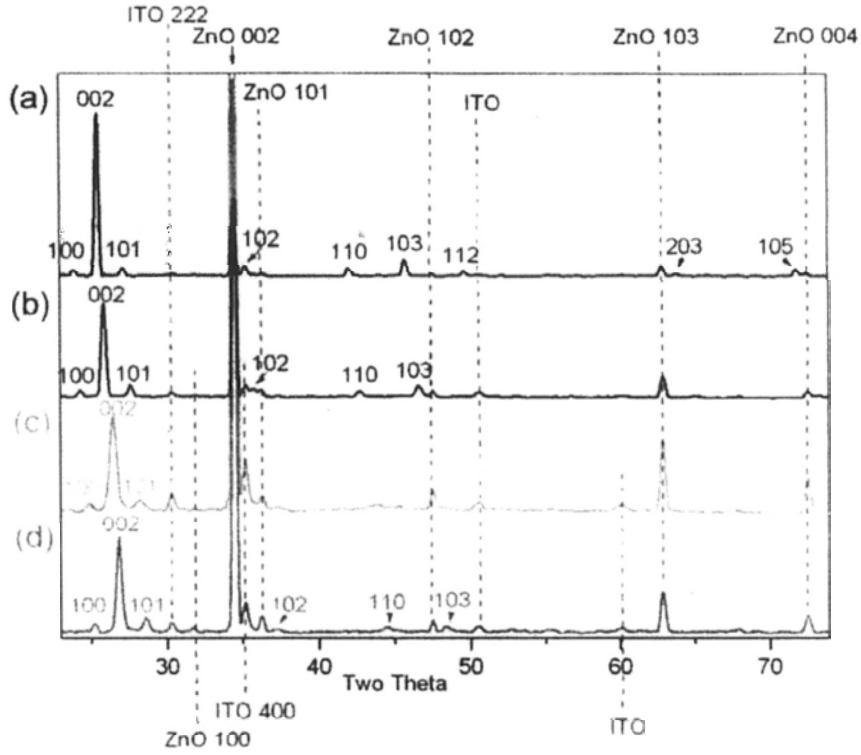

Figure 7- 2 XRD spectra taken from the four specimens: (a) sample 1, (b) sample 2, (c) sample 3, and (d) sample 4. Diffraction peaks from the crystalline ZnO core, the shell material, and the ITO on substrate are visible. Both the ZnO nanorod core and the shell have wurtzite structure.

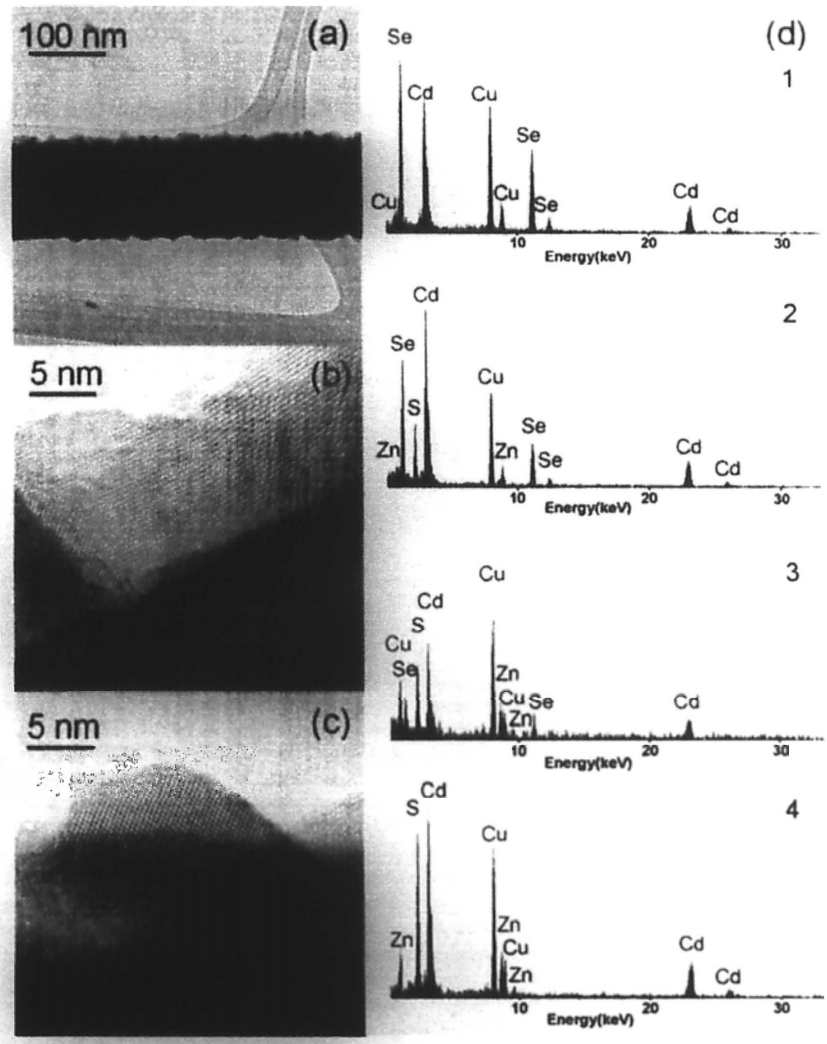

Figure 7- 3 (a) typical low magnification TEM image of the nanocable specimen. Diffraction contrast contributed by various domains of the shell layer suggests the polycrystalline nature of the shell. (b), (c) High resolution TEM images taken on the shell portion, showing the grain size's variation. (d) Typical EDX spectra taken on the shell regions of the four specimens using ~2 nm electron probe, revealing their composition. Small amount of Zn signal can always be found together with the S signal.

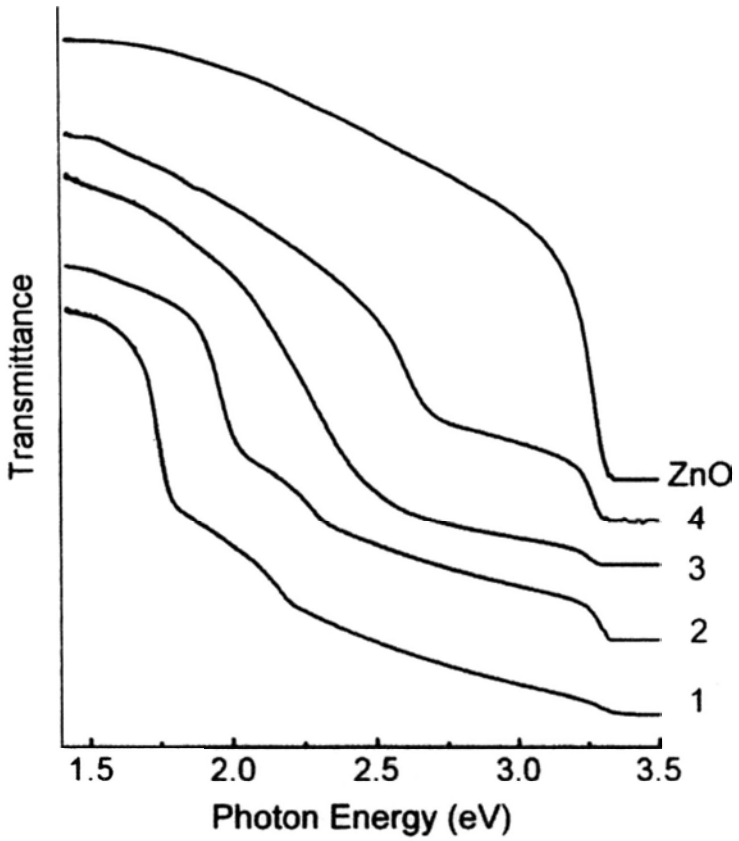

Figure 7- 4 Transmentence spectra taken from bare ZnO nanorod arrays on ITO/glass and the four nanocable specimens. From bottom to top of the figure, is spectrum for the (b) specimen #1, #2, #3, #4, and the bare ZnO nanorod arrays, respectively.

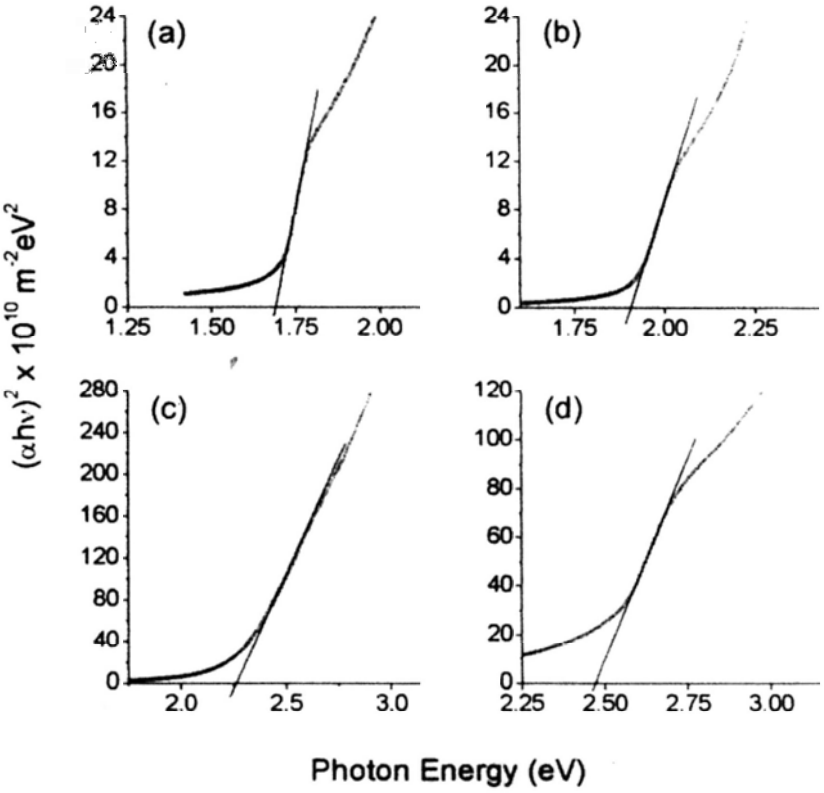

Figure 7- 5 Plots of $(\alpha h\nu)^2$ as a function of photon energy for the four nanocable specimens. By extrapolating the straight line portion of the plots to the energy axis at $\alpha=0$, the band gap value of the four alloy shells are estimated to be: (a) 1.69 eV for sample #1, (b) 1.90 eV for sample #2, (c) 2.26 eV for sample #3, and (d) 2.47 eV for sample #4.

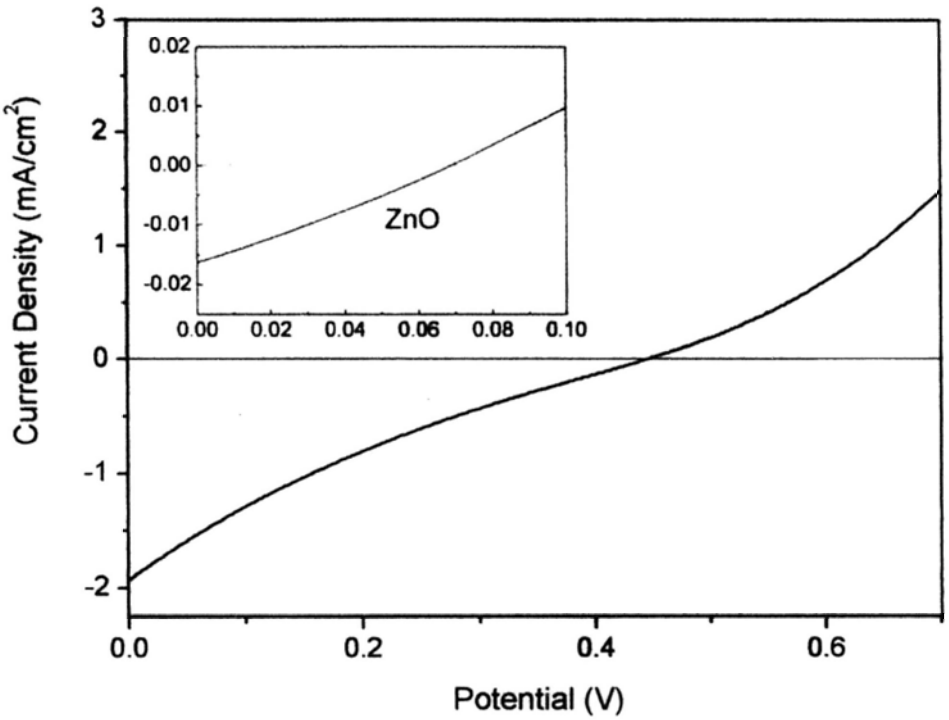

Figure 7- 6 J-V characteristic of one ZnO/CdSe nanocable solar cell, which were recorded while illuminating the cell with 100 mW/cm^2 simulated AM1.5 spectrum. The inset is the J-V characteristic of a cell assembled with bare ZnO nanorod arrays, which were recorded under the same illumination condition. Units of the inset are same as that of the large figure.

Chapter 8 Conclusions

The solution chemistry approach to synthesis ZnO nanorod arrays on Zn foil is convenient and low cost. Morphology and structural quality of the ZnO nanorods highly depend on their growth conditions, including the temperature and the relative concentrations of H_2O_2 and NaOH. This in turn provides us a way to control the growth. The average diameter of the ZnO nanorods in the array can be tuned from ~150 nm to ~20 nm. Larger-diametered nanorods possess higher band edge to defect emission ratio, indicating their better electronic structural quality.

Controllable growth of ZnO nanorod arrays can also be realized through a catalyst free vapor phase deposition approach. The concentration of ZnO vapor in the system plays an important role in determining both the substrate surface coverage and nanorods size. The employment of an additional small quartz tube in the original vacuum tube furnace setting could dramatically increase the areal coverage of the substrate by nanorod arrays. Larger-diametered nanorods that grow on higher temperature zone are found to have better electronic structural quality.

For future work, doping of the ZnO nanorods is worth to study, as doping plays a fundamental and important role in current semiconductor electronic industry. Successful and controllable doping will significantly promote the process to apply ZnO nanorods to various electronic devices. Both direct doping of the ZnO

nanorods during their growth and a secondary thermal diffusion doping method can be studied.

Although the green emission observed from the ZnO nanorods is commonly attributed to surface defect emission from the nanostructure, our experiment suggests that it is not necessarily true. Surface passivation fails to reduce the green emission significantly, indicating that surface defects of ZnO are not necessarily responsible for the green emission, but the interior structure quality of the ZnO nanorods decides the luminescence behavior.

Through the thermal evaporation method, a serials of core-shell ZnO / $Cd_xZn_{1-x}S_ySe_{1-y}$ nanocable arrays can be achieved. In the structure, single crystal ZnO nanorods are uniformly covered by wurtzite polycrystalline $Cd_xZn_{1-x}S_ySe_{1-y}$ layer. Band gap of the alloy shell varies with its composition changing, which provides a convenient way to tune the light absorption range in the nanocable structure. The type II band alignment between the ZnO core and the alloy shell enables effective photo-generated charge carrier separation and the single crystalline ZnO nanorod provides a direct electrical pathway for the photo-injected electrons. The prototype nanocable solar cells exhibit short-circuit current ~0.2 mA/cm^2 and open-circuit voltages of 0.45 V when illuminated with 100 mW/cm^2 simulated AM 1.5 spectrum.

Performance of the prototype solar cell is not so ideal, as it is also affected by many factors other than the nanocable structure, such as that related with the electrolyte and cell sealing technique. In addition, optimizing structural parameters of the nanocable to improve the cell performance requires further study. For example, a proper thickness of the polycrystalline alloy layer for enough light absorption and less carrier scattering loss in transport; and similarly, an optimal length of the ZnO nanorods, as the nanorods serve as support for the light absorber. It is believed that the nanocable solar cell would exhibit its superiority in future.

References

[1] Özgür, Ü.; Alivov, Y. I.; Liu, C.; Teke, A.; Reshchikov, M. A.; Doğan, S.; Avrutin, V.; Cho, S.-J.; Morkoç, H.; *J. Appl. Phys.* **2005**, *98*, 041301.

[2] Harada, Y.; Hashimoto, S. *PHYSICAL REVIEW B* **2003**, *68*, 045421.

[3] Wang, Z. L. *J. Phys.: Condens. Matter* **2004**, *16*, R829.

[4] He, J. H.; Hsin, C. L.; Liu, J.; Chen, L. J.; Wang, Z. L. *Adv. Mater.* **2007**, *19*, 781.

[5] Matsuu, M.; Shimada, S.; Masuya, K.; Hirano, S.; Kuwabara, M. *Adv. Mater.* **2006**, *18*, 1617.

[6] Wang, X.; Song, J.; Summers, C. J.; Ryou, J. H.; Li, P.; Dupuis, R. D.; Wang, Z. L. *J. Phys. Chem. B* **2006**, *110*, 7720.

[7] Wang, X.; Song, J.; Li, P.; Ryou, J. H.; D, R.; Dupuis; Christopher; Summers, J.; Wang, Z. L. *J. AM. CHEM. SOC.* **2005**, *127*, 7920.

[8] Yang, J.; Liu, G.; Lu, J.; Qiu, Y.; Yang, S. *Applied Physics Letters* **2007**, *90*, 103109.

[9] Michael H. Huang; Yiying Wu; Henning Feick; Tran, N.; Weber, E.; Yang, P. *Adv. Mater.* **2001**, *13*, 113.

[10] Zhang, Y.; Dai, Y. In *Nanowires and Nanobelts - Materials, Properties and Devices*; Wang, Z., Ed. 2004; Vol. II, p 139-156.

[11] Greene, L. E.; Law, M.; Goldberger, J.; Kim, F.; Johnson, J. C.; Yanfeng Zhang; Saykally, R. J.; Yang, P. *Angew. Chem. Int. Ed.* **2003**, *42*, 3031.

[12] Loh, K. P.; Chua, S. J. In *Molecular Building Blocks for Nanotechnology: From Diamondoids to Nanoscale Materials and Applications*; Springer Berlin / Heidelberg: 2007.

[13] H. J. Fan; Werner, P.; Zacharias, M. *Small* **2006**, *2*, 700.

[14] Xudong Wang; Song, J.; Wang, Z. L. *J. Mater. Chem.* **2007**, *17*, 711.

[15] Lori E. Greene; Matt Law; Tan, D. H.; Max Montano; Josh Goldberger; Gabor Somorjai; Yang, P. *Nano Lett* **2005**, *5*, 1231.

[16] Djurišić, A. B.; Leung, Y. H.; Tam, K. H.; Ding, L.; Ge, W. K.; Chen, H. Y.; Gwo, S. *Appl. Phys. Lett.* **2006**, *88*, 103107.

[17] Tam, K. H.; Cheung, C. K.; Leung, Y. H.; Djuris˘ic´, A. B.; Ling, C. C.; Beling, C. D.; Fung, S.; Kwok, W. M.; Chan, W. K.; Phillips, D. L.; Ding, L.; Ge, W. K. *J. Phys. Chem. B* **2006**, *110*, 20865.

[18] D. Li; Leung, Y. H.; Djurišiæ, A. B.; Liu, Z. T.; Xie, M. H.; Shi, S. L.; Xu, S. J.; Chan, W. K. *Appl. Phys. Lett.* **2004**, *85*, 1601.

[19] Korsunska, N. O.; Borkovska, L. V.; Bulakh, B. M.; Khomenkova, L. Y.; Kushnirenko, V. I.; Markevich, I. V. *J. Luminescence* **2003**, *102-103*, 733.

[20] Vanheusden, K.; Seager, C. H.; Warren, W. L.; Tallant, D. R.; Voigt, J. A. *Appl. Phys. Lett.* **1996**, *68*, 403.

[21] Ir H. He; Cheng L. Hsin; Jin Liu; Lih J. Chen; Wang, Z. L. *Adv. Mater.* **2007**, *19*, 781.

[22] Wang, Z. L.; Song, J. H. *Science* **2006**, *312*, 242.

[23] Hannes Kind; Haoquan Yan; Benjamin Messer; Matthew Law; Yang, P. *Adv. Mater.* **2002**, *14*, 158.

[24] Boyle, D. S.; Govender, K.; O'Brien, P. *Chem. Commun* **2002**, 80.

[25] Mende, L. S.; Driscoll, J. L. M. *Materials today* **2007**, *10*, 40.

[26] Wang, Z. L. *J. Phys.: Condens. Matter* **2004**, *16*, R829.

[27] Leschkies, K. S.; Divakar, R.; Basu, J.; Enache-Pommer, E.; Boercker, J. E.; Carter, C. B.; Kortshagen, U. R.; Norris, D. J.; Aydil, E. S. *Nano Lett* **2007**, *7*, 1793.

[28] O'Regan, B.; Gratzel, M. *Nature* **1991**, *335*, 737.

[29] Gratzel, M. *Nature* **2001**, *414*, 338.

[30] Wang, K.; Chen, J.; Zhou, W.; Zhang, Y.; Yan, Y.; Pern, J.; Mascarenhas, A. *Adv. Mater.* **2008**, *20*, 3248.

[31] Furube, A., et al. *J. Phys. Chem. B* **2003**, *107*, 4162.

[32] Katoh, R., et al. *J. Phys. Chem. B* **2004**, *108*, 4818.

[33] Reimer, L. *Scanning Electron Microscopy*; Springer-Verlag: New York, 1985.

[34] Reimer, L. *Transmission Electron Microscopy*; Springer-Verlag: New York, 1997.

[35] Williams, D. B.; Carter, C. B. *in Transmission Electron Microscopy*; Plenum press: New York, 1996.

[36] NUFFIELD, E. W. *X-RAY DIFFRACTION METHODS*; JOHN WILEY & SONS, INC.: NEW YORK, 1996.

[37] Yacobi, B. G.; Holt, D. B. *Cathodoluminescence Microscopy of Inorganic Solids*; Plenum Press: New York and London, 1990.

[38] L. Shi; Y.M. Xu; Li, Q. *Appl. Phy. Lett.* **2007**, *90*, 211910.

[39] Shi, L.; Xu, Y. M.; Hark, S.; Liu, Y.; Wang, S.; Peng, L.-m.; Wong, K.; Li, Q. *Nano Lett.* **2007**, *7*, 3559.

[40] Xu, F.; Lu, Y.; Xie, Y.; Liu, Y. *J. Phys. Chem. C* **2009**, *113*, 1052.

[41] Ostwald, W. *Lehrbuch der Allgemeinen Chemie*; Leipzig, Germany, 1896; Vol. 2.

[42] Brice, J. C. *Crystal Growth Processes*; Halsted Press, 1986.

[43] This work was finished by my group mate Mr. Zhu Haojun

[44] Batson, P. E. *Nature* **1993**, *366*, 727.

[45] Tian, H. F.; Yang, H. X.; Zhang, H. R.; Y. Li; H. B. Lu; and J. Q. Li *PHYSICAL REVIEW B* **2006**, *73*, 075325.

[46] Z. H. Zhang; H. H. Liu; J. K. Jian; K. Zou; and X. F. Duan *Appl. Phys. Lett.*

2006, *88*, 193101.

[47] Ya. I. Alivov; M. V. Chukichev; and V. A. Nikitenko *Semiconductors* **2004**, *38*, 31.

[48] N. Y. Garces; L. Wang; L. Bai; N. C. Giles; Halliburton, L. E.; and G. Cantwell *Appl. Phys. Lett.* **2002**, *81*, 622.

[49] R. Dingle *Phys. Rev. Lett.* **1969**, *23*, 579.

[50] K. Vanheusden; C. H. Seager; W. L. Warren; D. R. Tallant; and J. A. Voigt *Appl. Phys. Lett.* **1996**, *68*, 403.

[51] N.O. Korsunska; L.V. Borkovska; B.M. Bulakh; L.Yu. Khomenkova; V.I. Kushnirenko; and I.V. Markevich *J. Luminescence* **2003**, *102-103*, 733.

[52] Juan Wang; Xipo An; Quan Li; and R. F. Egerton *Appl. Phys. Lett.* **2005**, *86*, 201911.

[53] This work was finished by my group mate Mr. Zhu Haojun

[54] Wang, X.; Gao, P.; Li, J.; Summers, C. J.; Wang, a. Z. L. *Adv. Mater* **2002**, *14*, 1732.